AIAA Journal, Volume 61, Issue 4, April 2023, pp. 1735-1748
DOI:10.2514/1.J062033

Closed-form analytical approach for calculating noise contours of directive aircraft noise sources

D. C. Amargianitakis *, R. H. Self † and A. P. Synodinos‡
Institute of Sound and Vibration Research, University of Southampton, Southampton, Hampshire, SO17 1BJ, United Kingdom

A. R. Proença§
Applied Aerodynamics Group, School of Aerospace, Cranfield, Bedford, MK43 0AL, United Kingdom

A. J. Torija¶
Acoustics Research Centre, University of Salford, Manchester M5 4WT, United Kingdom

This paper extends the simplified airport noise model RANE (Rapid Aviation Noise Evaluator) [Torija et al. 2017], adding capability of including fully non-isotropic noise sources. This extended tool, RANE v2, is developed as a part of multidisciplinary acoustic assessment of novel aircraft, in order to produce ground contours around airports and helipads. Version 2 extends the capability of RANE to highly directional sources and aircraft to accommodate predictions of future air vehicles implementing propulsion systems solution with inherent directional properties. The model uses three-dimensional noise emission surfaces around a series of discretised segments that represent the aircraft flightpath. The main inputs are the sources' Sound Power Level (PWL) which are manifested through a noise radius, the distance from the flightpath at which a level is observed; and the source three-dimensional directivity. The directivity function may take analytical or numerical form, allowing for experimental data inputs. This paper demonstrates the use of Spherical Harmonics as a form of directivity function with a closed-form analytical solution for calculating the noise exposure contours. Results and comparison against the Federal Aviation Administration's Aviation Environmental Design Tool (AEDT) module for Helicopter Community Noise indicate that exposure contour coordinates can be estimated for high and low noise exposure levels. The incorporation of source directivity allows for the assessment of lateral attenuation, engine installation effects and transition operations (for vertical to horizontal flight and vice versa) via the assumption of individual source directivities and therefore complex noise surfaces. As a consequence of the analytical nature of the model, low computational requirements allow for fast exploration of

*PhD Student, ISVR, University of Southampton
†Professor, ISVR, University of Southampton, Southampton, Hampshire, SO17 1BJ, United Kingdom
‡Visiting Academic, ISVR, University of Southampton
§Lecturer in Aerodynamics, Applied Aerodynamics Group, School of Aerospace, Cranfield University
¶Lecturer in Acoustical Engineering, Acoustics Research Centre, University of Salford

the design space and parametric studies, with minimal input requirements. The capabilities of RANE v2 are demonstrated by predicting noise footprints for three helicopters, each of different size, performance, and directivity characteristics.

Nomenclature

A	=	Contour area
A_T	=	Total noise contour area due to the total of N segments
d	=	Shortest distance from an observation point to a flight path segment
d_p	=	Perpendicular distance from an observation point to the flight path (slant distance)
d_λ	=	Scaled distance
h	=	Altitude
ini,end	=	Limits of integration
l	=	Perpendicular distance from an observation point to the ground track
len	=	Length of the noise contour
L	=	Event sound-level (scale undefined)
L_E	=	Single event sound exposure level determined from NPD database
L_E	=	Single event sound exposure level (SEL)
$L_{eq,T}$	=	Energy-equivalent sound-level integrated over the period T
L_{max}	=	Maximum sound-level during an event
P	=	Power-setting parameter in NPD variable $L(P, d)$
Q	=	Distance from start of the segment to closest point of approach
R	=	Noise Radius
s	=	Segment length
$\mathbf{S}$	=	Orthogonal matrix
T_0	=	Reference time for integrated sound level
$\mathbf{U}$	=	$(u\ v\ w)^T$, position vector
v	=	Airspeed
v_{ref}	=	Reference airspeed for which NPD data are defined
$\mathbf{X}$	=	$(x\ y\ z)^T$, position vector
α	=	Parameter used for calculation of the finite segment correction ΔF
β	=	Elevation angle of aircraft relative to ground plane
γ	=	Inclination angle

θ = Polar directivity angle

φ = Azimuthal directivity angle

ϕ = Depression angle

ψ = Angle of rotation in the horizontal plane

$\Lambda(\beta, l)$ = Lateral attenuation adjustment

$\Lambda(\beta)$ = Long range air-to-ground lateral attenuation Λ_y (Orthogonal) rotation matrix

Δt = Time increment

ΔI = Engine-installation effects adjustment

Δv = Duration adjustment

$\Delta x, \Delta y$ = Displacement in the x and y directions, respectively

Δx = Displacement in the x dimension as a consequence of the different inclination angles (γ)

Subscripts

0 = Baseline Aircraft

a = Aircraft

i = Individual noise source

j = Flight track; individual parameter influencing noise source i

k = Individual flight track segment

n = Common flight track segments for the whole aircraft fleet

m = Number of aircraft movements

x, y, z = Orthogonal coordinate system for each kth flightpath segment

X, Y, Z = Common orthogonal coordinate system for all k flightpath segments, Airport system

u, v, w = Orthogonal coordinate system with the u axis is aligned with the kth flightpath segment.

θ, φ, r = Spherical coordinate system used for NPD flyover procedures and lateral attenuation definition.

d_p, φ, u = Cylindrical coordinate system for each kth flightpath segment

I. Introduction

The aviation industry is reaching a turning point. Environmental impact concerns and the push for zero emissions is driving government agencies and strategists to form detailed plans of how the civil aviation industry will adapt and transform [1]. In particular, the UK government and industry through funding a series of projects [2, 3] are leading the way in developing novel vehicle technologies covering drones, advanced air mobility vehicles and zero-carbon regional aircraft with the aim of addressing UK Civil Aviation Authority and public concerns regarding sustainability, noise, intrusion and safety.

Leveraging the advancement of electrical and hydrogen (H2) propulsion systems and battery technologies will slowly allow manufacturers to introduce new hybrid or fully electric designs to the market in the form of regional zero emission aircraft. Various recent studies have explored the possibilities and challenges of such architectures, along with industry requirements in order to accomplish this transition [4–7]. Research topics encompass everything from large long-haul aircraft to short-haul, regional, and even Urban Air Mobility (UAM) vehicles. The introduction of these new categories of aircraft, along with the existing increase in air-traffic, impose a very serious problem to the noise impact around airports and urban areas where these novel aircraft will most likely operate [8].

Urban Air Mobility (UAM) or Personal Air vehicles is a rising section of the aviation market seeking to provide on-demand aviation services and solutions. A number of hurdles exist in the development of this sector: aviation safety, airworthiness, operating and maintaining costs, airspace integration, aircraft noise and emissions and finally community acceptance [9]. As UAM aims to fill a market gap, at the same time it creates an entirely new aviation sector. Innovative technologies such as electric propulsion allow for aircraft/rotorcraft to perform operations and manoeuvres not before capable in the aviation world. Unfortunately, along with these capabilities comes a caveat. Regulations and certification procedures for such operations in urban environments have yet to be fully defined, however the European Union Aviation Safety Agency (EASA) published the Prototype Technical Design Specifications for Vertiports [10]. This document provides guidance to facilitate the safe design of vertiports for future eVTOL operations. Current regulations will need to be amended or even replaced with newly defined ones. The process of defining rules and regulations, and integrating such vehicles in an already existing transport and Air Traffic Control (ATC) infrastructure forms a complex problem in and of itself. It requires a full understanding of the capabilities of the vehicles along with all risks associated with all engineering components in order for safe operation to be accomplished. Additionally, the impact of vehicles on their operation environment must also be understood. In densely populated urban areas noise may strongly influence the regulations decided upon and may greatly affect the introduction of UAM vehicles. Therefore, the design and prediction capabilities of noise and airport models for these vehicles is a top priority.

The development of hybrid/electric propulsion systems allows for novel configurations of vehicles. Vertical Take-off and Landing (VTOL) plus cruise configurations become possible due to the size and lower complexity of electric motors. Distributed Electric Propulsors (DEP) along the airframe and wing assemblies leverage different set-ups to allow for benefits of VTOL capabilities while also harnessing the efficiency of horizontal fixed-wing flight. Enabling the rotation of propellers, ducted fans, and rotors during flight in order for the vehicle to transition from one operating state to another, creates a series of previously unanswered questions in many disciplines such as flight mechanics, controls and, aeroacoustics and noise emission.

For airport noise and aircraft noise source analysis to be integrated and contribute to the preliminary design of these aircraft, the restrictive nature of today's tools must be overcome. The ECAC modeling methodology presented in [11] and the Aircraft Noise and Performance (ANP) database [12] are based around the operation of conventional

fixed-wing aircraft. The FAA's Aviation Environmental Design Tool (AEDT) [13] implements this methodology along with extensions for a number of civil and military helicopters using an equivalent database that includes helicopter operations (Base of Aircraft DAta, BADA [14]). Although this methodology allows for the generation of exposure contours around airports and helipads, it is very limited by the inputs and experimental data available. No modularity exists in the definition of noise sources and especially their complex radiation patterns.

Grid-point tools, such as AEDT or ANCON (Aircraft Noise Contour Model [15]), depend on the existence of a substantial quantity of data that describes, principally, the airport and the air traffic using it - in terms of the aircraft types, numbers, routeings and operating procedures. In order for these databases to be extended and ECAC CEAC Doc 29 modeling procedures to be applied for novel configurations of vehicles, expensive and time consuming measurement campaigns are required. In addition to noise data, detailed operation and performance data are required as inputs for noise exposure contour generation. This postpones airport and community noise analysis until finalised variants of the designs are manufactured and flight tested.

RANE v2 forms the airport noise tool component of a larger high-level framework for the analysis and exploration of air vehicle design space in terms of noise output and community noise exposure. The framework, and in particular RANE v2, addresses the current gap in noise prediction during the conceptual and preliminary design phases of air-vehicles, whereby assessment of community noise is bypassed. The detailed inputs defining the many aeroacoustic sources and how they vary with operation/performance, as well as detailed flight trajectory data are unattainable at the conceptual phase of design add to the complexity of assessing noise impact. Therefore, what differentiates RANE from other airport noise tools, is the intended application and futures such as: i. high-level fast calculations able to keep up with the vast amount of concepts and design iterations, ii. high-level fast calculations able to keep up with the vast amount of concepts and design iterations, iii. assess community exposure and fleet scale operations around airports as a function of design iteration. It is mainly used as an academic research tool to provide acoustic consultations for projects that aim to design the future zero emission aviation market; and not aimed at replacing or competing with the current complex grid-point methods used to model detailed airport scenarios as a part of operation noise monitoring and regulation compliance. RANE v2 (Rapid Aviation Noise Evaluator version 2), aims to further the capabilities of RANE [16].

Although RANE proved that for simple single runway scenarios, changes in airport noise contour areas can be estimated with minimal uncertainty compared against grid-point calculation methods, its main assumption of omnidirectional sources, limits its capabilities to conventional turbofan airliner designs (the dominant turbofan aircraft noise sources contribute to an approximately omnidirectional nature of emission [17]). Furthermore, conventional approach, landing, take-off and climb operations are implemented, allowing for the more complex operations such as vertical take-off and landing (VTOL), hovering and mid-air direction reversal. RANE v2 is based on the work of Stewart and Carson (1979) [18], however the assumption of an isotropic source is disregarded. RANE v2 expands

the assumption of an isotropic source to the ability to define the aircraft noise source characteristics in more detail. The aircraft is described by a lumped noise source made up of contributions of individual component level sources. The lumped source is characterised by a Sound Power Level (PWL) and a three-dimensional directivity function. A spherical harmonic expansion is used to define the directive properties of the aircraft as a whole. The concept of noise exposure surfaces is introduced and explicitly defined and their calculation is then performed analytically. The pre-integrated noise surfaces can then be applied to discretised aircraft flightpaths during take-off and landing operations for conventional fixed-wing aircraft or VTOL operations, characteristic of helicopters and UAM air vehicles.

The structure of the present article is as follows. Initially, a theoretical background is provided relative to the flyover procedure as implemented by pre-integrated models such as conventional grid method (ECAC Doc29 [11]) and RANE, identifying the key differences between the two. Section III then describes the key contributions of version 2 of RANE, that being the implementation of three-dimensional source, that allows independent directional characteristics in the azimuth and polar directions. Referencing the flyover procedure, the generation of quadric [19]noise surfaces in three-dimensional space is described. These represent iso-surfaces of constant sound exposure levels and describe cumulative noise levels resulting from single event aircraft movements in three-dimensional space. Section III.B describes how the whole airport noise model is set-up in an common ground coordinate system. Specifically, details are given on the discretisation of continuous flightpaths into finite segments; the generation of noise surfaces for each segment corresponding to geometrical parameters defining the segments and aircraft operational parameter along it; and the translation and rotation of the contour contributions of each segment onto the common airport coordinate system.

Section IV and Vintroduce the use of spherical harmonics that allows the definition of a three-dimensional source and the use of quadratic and cubic splines to connect contour segments when discontinuity arises, respectively. Bench-marking and demonstration of the capability of RANE v2 is presented in Section VI through the comparison to two different prediction models. Finally, the two main errors due to assumptions made are discussed, along with the currently implemented corrections and how the accuracy of these could be improved for future calculations.

II. Flyover Procedure

A. Conventional grid-point models

Current airport noise tools base their calculations on experimentally obtained noise data and, after a series of interpolations, extrapolations, and corrections, provide predictions of noise as a result of aircraft single or cumulative (aircraft fleets) events. The data typically consists of Noise-Power-Distance (NDP) curves generated by manufacturers according to regulation in support of, noise contour calculation. NPD curves along with flightpath data are the main input parameters for airport noise exposure tools. The flightpath data holds all the geometry/distance information with respect to stationary observer locations on the ground, whereas NPD curves carry the noise source characteristics

information. Due to the complexity and cost involved in the generation of experimental NPD curves, the actual source characteristics captured within the curves is limited to the PWL emitted by the source (aircraft). Therefore, NPDs provide the relationship between the PWL of a given aircraft at a reference flight speed and atmosphere, and the slant distance from the flightpath at a number of engine power settings. This relation is captured in terms of various aircraft noise metrics, commonly maximum sound pressure level, $L_{\mathrm{A,max}}$, sound exposure level (SEL) and effective perceived noise levels (EPNL) [20].

As a result, important information about the characteristics of the source is lost. The most evident example is that of the source directivity. As the flyover occurs the observer (experimental microphone, sitting at a location directly under the flightpath) experiences noise emitted at a constant azimuthal angle, $\varphi = 0$, as seen in Figure 1, therefore all noise emitted by the source at other azimuthal angles in neglected in the generation of NPD curves. Figure 2 illustrates a typical experimental flyover test setup.

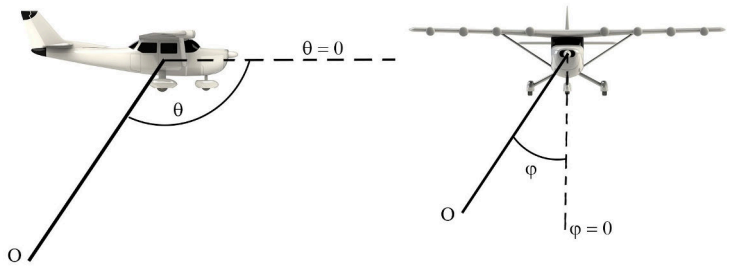

Fig. 1 Polar and azimuthal angles defining observer location. Adapted from [21]

To manage this issue, airport noise models introduce a series of source related correction factors. The contribution, therefore, from one flightpath segment to the single event sound exposure level at any observation point is calculated as follows:

$$L_E = L_E(P, d) + \Delta I(\varphi) - \Lambda(\beta, l) \tag{1}$$

where $L_E(P, d)$ is the SEL due to an aircraft of power setting P at a slant distance d emitting $L_w(P)$. The correction factors $\Delta I(\varphi)$ correspond to engine installation effects, which varies depending on the propulsion systems and the mounting location of said system. The lateral attenuation, $\Lambda(\beta, l)$, adjustment is a function of the lateral radiation characteristics of the source and interference effects caused by reflection off the ground (refraction caused by atmospheric conditions also strongly influences lateral attenuation). Both correction factors are given in terms of emission angles (see Fig. 1) and are usually modelled by empirical or semi-empirical methods [22],[23].

To accompany these source related corrections, other single event correction terms are applied to account for difference in aircraft speed, sound propagation (atmospheric and ground effects) and finite segments to name a few. Information and exact modeling procedures of the grid-point airport noise model may be found in ECAC Doc 29[11],

where the standardised procedures of flightpath discretisation, grid generation and noise data extrapolation is explained in full detail.

Characteristic examples of airport noise tools following the grid-point method are the FAA's AEDT [13, 24] the successor to the FAA's original INM (Integrated Noise Model). NASA is currently working on expanding the capability of AEDT to UAM and AMM vehicles [25, 26] and in the process developing a suite of tools capable of characterising individual sources using high-fidelity CFD or analytical codes (eg. PSU-WOPWOP [27, 28]) all the way to generating noise exposure contours. European tools that implement grid-point methodology, using both the pre-integrated as well as simulation approach (see Doc29 for differences in modeling approach) are Eurocontrol IMPACT [29] and STAPES (SysTem for AirPort noise Exposure Studies) as is the UK's ANCON2 [15] based on the original ANCON model. A review of most current and previous airport noise models was performed by Eurocontrol as a part of Sixth framework programme Priority 1.4 Aeronautics and Space [30].

By introducing a three-dimensional directivity function, in the form of a spherical harmonic expansion, these empirical corrections may be included in the definition of the sources. This bypasses the need for applying the individual corrections to each observer location independently, as the corrections are included in the initial calculation of each noise surface of interest, further cutting down calculation times. As RANE solves for observer locations that experience a certain value of noise level, the conventional grid method empirical corrections applied to the levels at each observer location are not applicable. Therefore these corrections are inverted to the source coordinate frame and included in the implicit solution of the noise surface equation, through a correction to the noise radius. This results in the corrections being a function of the azimuthal angle, the already calculated noise radius and the segment inclination angle. This assumes that all observer locations that result from one segment's noise surface experience the same corrections. For realistic cases the granularity of the flightpath discretisation is already high to account for performance and trajectory geometry accuracy, therefore segments . In the case of long segments, additional discretisation points are introduced for these corrections alone.

B. Existing capability of RANE: Noise Surface Method

RANE [16] is built on the concept of pre-integrated noise exposure iso-surfaces surrounding the aircraft trajectory. The intersection of these iso-surfaces with the ground plane define the location of the noise exposure contours around an airport. The detailed procedure of how this is accomplished in the current version of RANE is briefly discussed.

The complex three-dimensional aircraft trajectory is discretised into a series of linear segments. Each of these segments is treated mathematically as an infinite straight and level flyover, at constant speed, power setting (usually measured through net thrust) and configuration (eg. flap, slat, landing gear) with a correction applied to account for the actual finite length of the that particular segment.

The procedure for calculating a noise surface for a single segment is as follows. Assume an aircraft flies along an

infinitely long flight path with fixed altitude and engine power setting, j, and at a constant velocity. As a noise source, the aircraft is treated as a single (lumped) directional source. This, therefore, allows the source to be totally defined using an acoustic sound power, W (or a PWL, L_w) and a directivity factor. The directivity factor is responsible of distributing the total amount of acoustic energy into different directions in three-dimensional space, allowing for aircraft to have different acoustical properties in the polar and azimuthal directions, defined as in Figure 1.

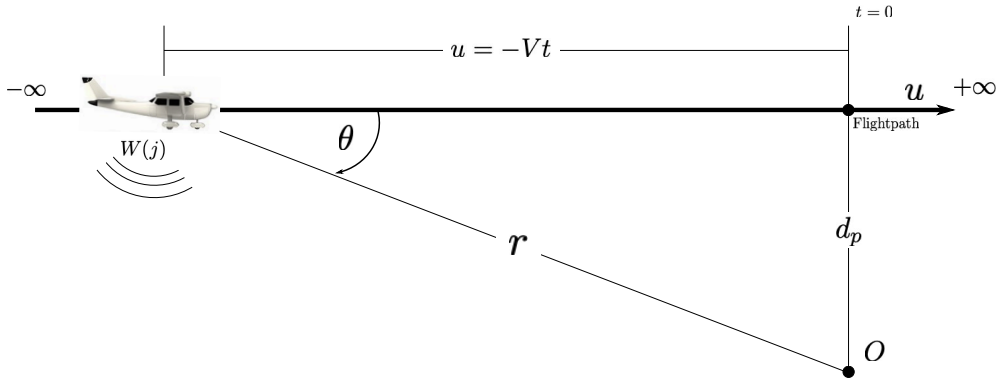

Fig. 2 Diagram of typical flyover procedure for obtaining NPD data.

In the case of the noise surface method it is important to clarify that the dependant variable of interest is the perpendicular distance d_p (Figure 2), while the noise sound exposure level, L_E serves as an independent variable. The slant distance from the flightpath at which a certain SEL is observed is also a direct function of the polar and azimuthal directive properties of the noise source performing the flyover.

Taking an omnidirectional source as an example, all observer locations O at perpendicular distance d_p and azimuthal angle $-\pi < \varphi < \pi$ experience the same SEL as the source properties and geometry of the flyover are identical. As we have assumed an infinite flyover, the problem is two-dimensional, meaning that irrelevant of the axial (u) position of the observer, if it has a perpendicular distance to the flightpath equal to d_p it will also experience the same SEL. Therefore, a cylindrical surface of observers experiencing the same exposure level is formed around the flightpath and, it is characterised by the perpendicular distance d_p. This is the approach used by RANE [16] and Stewart and Carson [18]

For an anisotropic source as in RANE v2, the perpendicular distance at which the same SEL occurs is a function of the azimuthal angle φ, therefore $d_p(\varphi)$. The infinite flyover however, still guarantees that d_p is independent of the polar angle θ. The resulting surface not longer has a circular cross-section, rather a cross section that depends in the initial source directivity function $D(\theta, \varphi)$.

We can define as constant SEL noise surfaces the observer locations around the flightpath that experience the same constant SEL as a result of an aircraft flying along an infinitely long straight flightpath. This three-dimensional surface is an 3D iso-surface contour of the SEL metric. When talking in terms of noise surfaces surrounding infinite flightpaths

the slant distance takes the name noise radius, R. For a directional sources, the noise radius of the observer locations will not be constant for a constant SEL noise surface. The procedure for calculating the variation of the noise radius as a function of the azimuth angle is detailed in Section III.

III. Analytical principles for directive source contour calculation

A. Noise Surfaces

Referring to Figure 2, let us assume that a test aircraft flies at a fixed altitude and engine power setting j, generating sound power $W(j)$ or $L_W(j)$. The resulting noise is measured at a location directly under the flightpath, denoted 'O', and hence the slant distance d_p, equals the altitude. At this point let us define a cylindrical coordinate system (u, φ, d_p) in which the reference axis u is aligned to the flightpath (Figure 2). This allows observer locations to be defined anywhere in three-dimensional space.

As the aircraft flies along this constant altitude flightpath its position with respect to the observer can be defined using the polar directivity angle θ and the slant distance alone. Therefore, we can define the instantaneous Sound Pressure Level observed at position O in terms of the acoustic sound power and the distance between the observer and the aircraft (source) at this point in time, r. It can be seen quite trivially that r is a function of θ and can be written as, $\sin\theta = d_p/r$. Therefore, we have:

$$L_p(\theta, \varphi, r) = 10 \log \left[\frac{WD(\theta, \varphi)}{r^2(\theta)} C \right] \tag{2}$$

An additional parameter $D(\theta, \varphi)$, has been introduced. The directivity factor as is called, is defined as the ratio of the sound intensity in the direction (θ, φ) and the mean intensity, $D(\theta, \varphi) = I(\theta, \varphi)/\bar{I}$. For the case of an omnidirectional source the directivity factor equals 1. C is a constant dependent on the reference pressure $p_{\text{ref}} = 20\mu\text{Pa}$ which represents the threshold of human hearing, $C = \rho c/(4\pi p_{\text{ref}}^2)$. As the noise surfaces we are interested in are essentially 3D contours of constant sound exposure levels.

At this point it will be useful to use the definition of the SEL noise metric and to distinguish it from other instantaneous noise metrics, as it is a key to the definition and derivation of the noise surfaces. The SEL or L_E is a continuous steady level, which over the period of 1 s contains equivalent total acoustic energy as the actual fluctuating (instantaneous) noise. Mathematically it can be calculated by integrating the instantaneous time history $L_P(t)$ as the aircraft performs the flyover. That is,

$$L_E = 10 \log \int_{-\infty}^{+\infty} 10^{\frac{L_P(t)}{10}} \, \mathrm{d}t \tag{3}$$

The integral in Equation 3 represents the SEL level calculated as a result of an event that is infinitely long (in time).

It is apparent however, that only a small portion of such an event is responsible for contributing the significant part of the total noise exposure at an observer location. It is common practise to only include that portion in noise calculations and measurements. The significant part duration is normally specified by incorporating suitable threshold levels at which the event start/end limits are triggered. A typical threshold level is 10 dB below $L_{\mathrm{A,max}}$ named the 10 dB down-time, t_{10} [11]. The finite segment error correction (Section VI.C.1) provides insight on how the noise exposure from finite sections are related to the infinitely long event and the integral in Equation 3.

Substituting Equation 2 into 3 and performing the following algebraic manipulations we have,

$$L_E = 10 \log \int_{-\infty}^{+\infty} \frac{W(j) D(\theta, \varphi)}{r^2} C \, \mathrm{d}t \tag{4}$$

From Figure 2, we introduce the substitution:

$$r^2 = d_p^2 + q^2 = d_p^2 + (-Vt)^2 \tag{5}$$

We can now perform the change in integration variable from t to θ using,

$$t = -\frac{d_p}{V \tan \theta} \tag{6}$$

$$\frac{dt}{d\theta} = \frac{d_p}{V \sin^2 \theta} \tag{7}$$

Therefore, the sound exposure level at the observer from the flyover in the time interval between $[-\infty, +\infty]$ can be expressed as:

$$L_E = 10 \log \frac{W(j) C}{V d_p} \int_0^{\pi} D(\theta, \varphi) \, \mathrm{d}\theta \tag{8}$$

The SEL at any observer O in space can be obtained by the expression in Equation 8. Independently of the dependence of D on the polar angle θ, as the single definite integral is evaluated with respect to θ, the azimuthal angle φ may be treated as a constant. Therefore, we essentially get an anti-derivative function $D_F(\theta, \phi)$ for which,

$$\frac{\partial D_F(\theta, \varphi)}{\partial \theta} = D(\theta, \varphi) \tag{9}$$

and the integral can then be evaluated as,

$$\int_0^{\pi} D(\theta,\varphi)\,\mathrm{d}\theta = \Big[D_F(\pi,\varphi) - D_F(0,\varphi)\Big]_0^{\pi} \\ = f(\varphi) \tag{10}$$

Substituting this into 8, and using the noise radius, R, nomenclature instead of the slant distance,

$$L_E = 10\log\frac{W(j)C}{VR}f(\varphi) \tag{11}$$

This indicates that for a directional source, the SEL at any observer location is a function of the azimuthal position of that observer with respect to the flightpath. The polar dependence has been eliminated, through the integration. Equation 11 also serves as the definition of the noise surface itself. To prove this, we begin by using the definition of the Cartesian flightpath coordinate system (u, v, w). The u axis (flight axis) of this coordinate system is aligned with the longitudinal axis of the cylindrical coordinate system (R, φ, u) previously used. The correspondence between the two systems is,

$$u = u, \quad v = R\cos\varphi, \quad w = R\sin\varphi \tag{12}$$

with

$$R^2 = v^2 + w^2 \tag{13}$$

Using Equation 11 and solving for R, we have,

$$R = \frac{W(j)C}{V10^{\frac{L_E}{10}}}f(\varphi) \tag{14}$$

Using the conversion from cylindrical coordinates to Cartesian,

$$v^2 + w^2 = \frac{W(j)C}{V10^{\frac{L_E}{10}}}f(\varphi) \tag{15}$$

The right-hand-side of Equation 15 is a function of azimuthal angle (observer lateral position), the equation is similar to that of a cylinder with central axis coincident with the flightpath with the major difference that the radius is not constant,

$$v^2 + w^2 = R_{iso}^2 D_\Lambda(\varphi) \tag{16}$$

R_{iso} represents the noise radius of an isotropic source of equal sound power, velocity and dB SEL contour requirement. As in RANE the R_{iso} is calculated using NPD databases using the power setting P, aircraft speed V and required SEL contour dB. As will be discussed later in this paper, $D_\Lambda(\varphi)$, the function responsible for the azimuthal radiation of the source can be inputted in various forms. Figure 3 shows a typical example of the resulting three-dimensional noise surface surrounding the flightpath. The various observer locations on the surface are indicated, highlighting the difference in slant distance with respect to the flight for a constant level SEL.

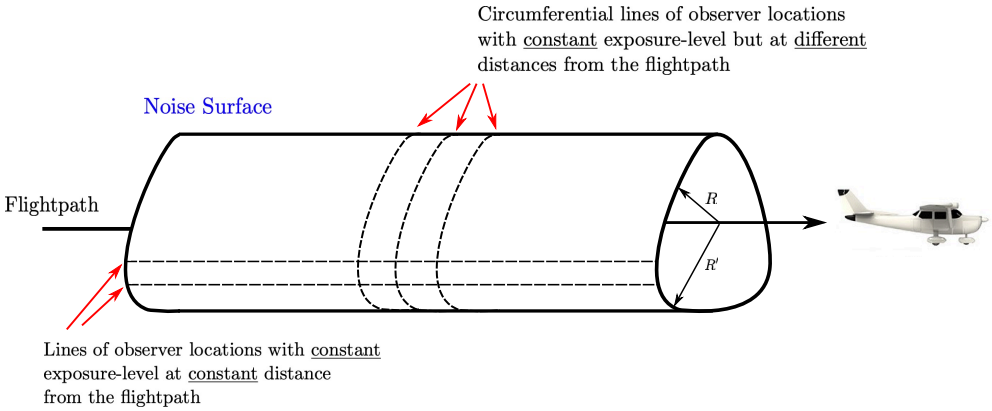

Fig. 3 Typical noise surface of an azimuthaly directional noise source. The cross section of the surface is no longer a circle, therefore constant exposure levels do not always occur at the same minimum distance from the flightpath.

It is more elegant and will prove useful to represent the noise surface is in matrix form. Equation 16 may be written in matrix form as,

$$\mathbf{U}^T\mathbf{S}\mathbf{U} = R^2 D_\Lambda(\varphi) \tag{17}$$

where $\mathbf{U} = (u\ v\ w)^T$ is the position vector and the orthogonal matrix,

$$\mathbf{S} = \begin{bmatrix} 0 & 0 & 0 \\ 0 & 1 & 0 \\ 0 & 0 & 1 \end{bmatrix} \tag{18}$$

The term $D_\Lambda(\varphi)$ can also be converted to the orthogonal (u, v, w) system by using Equations 12 to 9, giving $\mathbf{U}^T\mathbf{S}\mathbf{U} = R^2 D_\Lambda(u, v, w)$.

This result can be interpreted in two ways:

- All observer positions whose position is defined by the same azimuthal angle will experience the same exposure

level.

- The distance from the flightpath at which the same constant exposure level exists is now not equal to the slant distance R_{SL} for all observers, but it depends on the azimuthal position and therefore the result of the integration, $f(\varphi)$ in Equation 11.

B. Airport model: three-dimensional trajectory

A typical three-dimensional aircraft trajectory is modelled as a finite amount of straight-line segments. Way-points are positioned at the extremities of each of these line segments. Way-point 1 is the start of the take-off roll located at the origin of our (X, Y, Z) airport coordinate system; way-point 2 is lift-off and the general k^{th} segment is between the k^{th} and $(k + 1)$ way-points.

Each segment is characterised by the following parameters:

1) an inclination angle γ measured positive above the horizontal $X - Z$ plane.
2) a segment length s.
3) a distance R from the aircraft corresponding to the desired Sound Exposure Level (SEL) noise contour and specified power setting.
4) an angle ψ measured positive counter clockwise from the airport X axis to the segment.
5) a directivity function $D(\theta, \varphi)$ describing the sources directional radiation properties along that segment

Definitions of segment specific parameters can be seen in Figure 4, the definition of each segment within the airport frame (X, Y, Z) remain the same as in references [16, 18]. Each k^{th} flightpath segment is aligned with the u axis of the previously defined orthogonal segment coordinate system (u, v, w). Let us also define an orthogonal coordinate system (x, y, z), in which for each k flightpath segment x is the projection of the u axis on the ground horizontal plane, and the y axis is coincident with the v axis (rotation around the y axis).

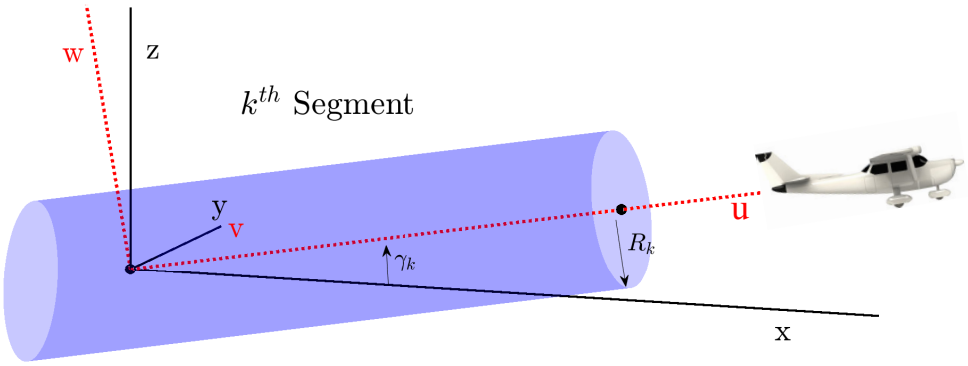

Fig. 4 Definition of the flightpath Cartesian and cylindrical coordinate systems for each segment k, with respect to the orthogonal projection system (x, y, z). Revised from [16].

As the noise surface is defined in the (u, v, w) coordinate system it must also be projected to the system defined by position vector $\mathbf{X} = (x\ y\ z)^T$. The transformation between the two vectors $\mathbf{U}$ and $\mathbf{X}$ is,

$$\mathbf{X} = \Lambda_y \mathbf{U} \tag{19}$$

where Λ_y is an orthogonal matrix given by,

$$\Lambda_y = \begin{bmatrix} \cos\gamma & 0 & -\sin\gamma \\ 0 & 1 & 0 \\ \sin\gamma & 0 & \cos\gamma \end{bmatrix} \tag{20}$$

Thus we transform Equation 17, which defines our noise surface, using Equation 19, gives,

$$\mathbf{X}^T \Lambda_y \mathbf{S} \Lambda_y^T \mathbf{X} = R_{iso}^2 D_\Lambda(x, y, z) \tag{21}$$

where $D_\Lambda(x, y, z)$ is the transformed version of the azimuthal directivity function.

The 2D noise contour is then determined by the intersection of the three-dimensional noise surface in terms of the coordinate system $(x\ y\ x)$ with the ground horizontal plane, $X = (x\ y\ 0)$. The final contour is stitched together on to the airport coordinate system ground plane (X, Y) taking into account the contributions of each of the n^{th} segments using a series of translations and rotations for each of them *. This process is almost identical to RANE [16] therefore it will not be reproduced here. An illustration of the processes may be seen in Figure 5. The three individual noise surfaces (green, purple and yellow) may be be seen in Figure 5a, in the airport frame. Figure 5b shows the resulting contours of said noise surfaces after the intersection with the airport ground plane (X - Y) has been taken.

IV. Three-dimensional source directivity

A. Modeling Source directivity function using Spherical Harmonics

In order to generate the procedure for calculating the noise radius R of a directive source it will prove effective to assume that the directivity function is expanded in terms of Spherical Harmonics. We define the complex sound emission in the direction defined by the two angles θ and ϕ using a decomposition into contributions of spherical harmonics:

$$D(\theta, \varphi) = \frac{1}{N} \left| \sum_{\ell=0}^{n} \sum_{m=0}^{\ell} A_\ell^m Y_\ell^m(\theta, \varphi) \right|^2 \tag{22}$$

*After projecting each noise surface into the $\mathbf{X}$ frame, a rotation about the y-axis is performed over angle γ_k, and one about the z-axis over angle ψ_k to align the x-axis with the corresponding segment of the discretized flightpath.

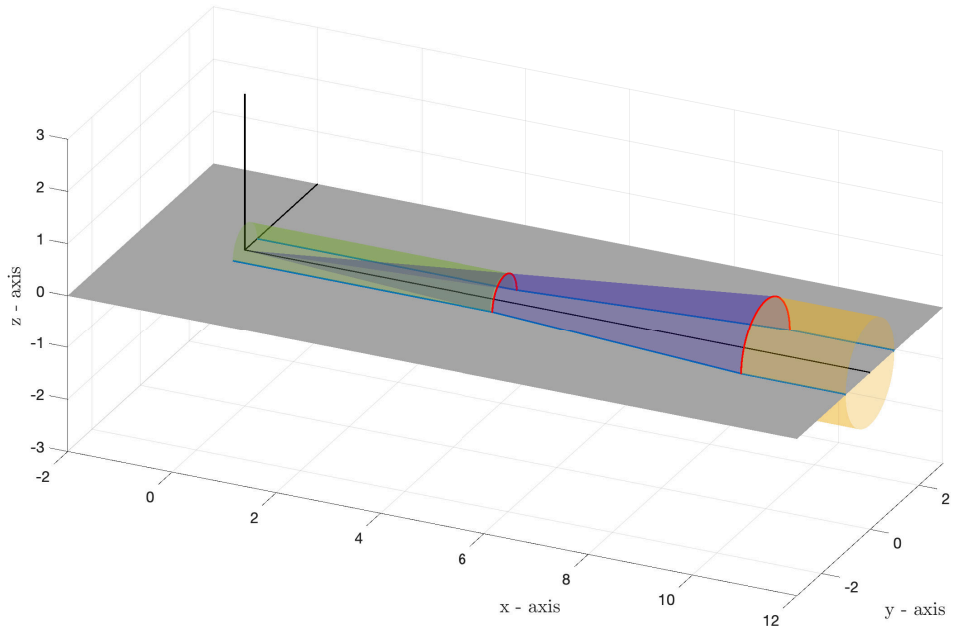

(a) Illustration of three surfaces corresponding to three different flightpath segments. Each segment has a different noise radius corresponding to a varying power setting. The intersection with the ground plane (gray) is also pointed out (blue line).

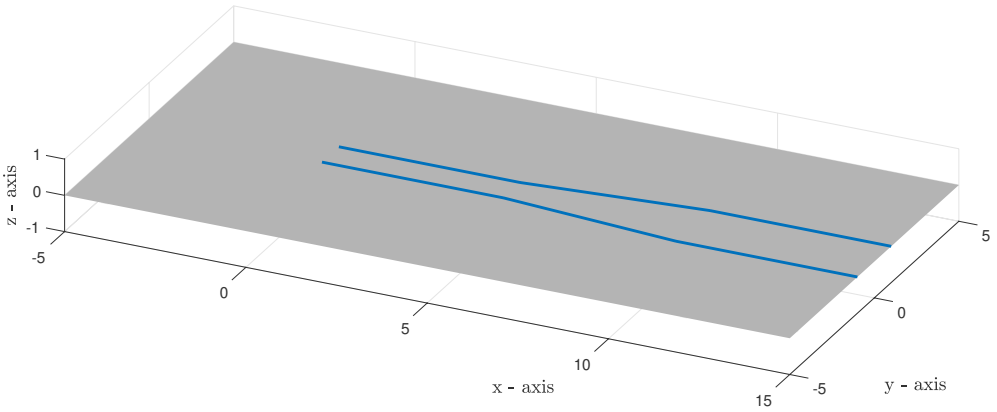

(b) Noise footprint on the ground plane as a result of the intersection of the noise surfaces with it.

Fig. 5 Demonstration of the generation of the two-dimensional ground contour as a result of the intersection between the three-dimensional noise surface and the ground plane.

The directivity function, $D(\theta, \varphi)$ is given in terms of different contributions of Spherical Harmonics Y_ℓ^m and coefficients A_ℓ^m describing the magnitude of contribution of each harmonic. Using the conventional notation, spherical harmonics are defined on a spherical coordinate system, with angles θ, φ representing the colatitude and longitude, respectively. The colatitude θ, is defined from 0 on the flightpath in front of the aircraft to π on the flightpath behind the aircraft ($0 \leq \theta \leq \pi$), whereas the longitude φ or azimuth may assume all values ($0 \leq \varphi \leq 2\pi$) around the flightpath (same convention as used to define observer locations in Figure 1).

As we have introduced an orthogonal flightpath coordinate system (u, v, w), the spherical harmonics coordinate system (θ, φ) is related to it by,

$$\varphi = \arctan\left(\frac{v}{u}\right), \quad \theta = \arccos\left(\frac{w}{\sqrt{u^2 + v^2 + w^2}}\right) \tag{23}$$

or reversely,

$$u = \sin\theta\cos\varphi, \quad v = \sin\theta\sin\varphi, \quad w = \cos\theta \tag{24}$$

The directivity function is a ratio of the sound intensity in the direction (θ, φ) and the mean intensity. Therefore, to retain this property we must ensure the $D(\theta, \varphi)$ is normalised in a way, so the overall acoustic power emitted is unaffected. This condition is satisfied if the integration over the entire spherical surface surrounding the source returns the power of the source,

$$\int_S \frac{WD_s}{4\pi}\,\mathrm{d}S = W(j) \tag{25}$$

or in terms of the directivity function, $D(\theta, \varphi)$,

$$\int_S D(\theta, \varphi)\,\mathrm{d}S = 1 \tag{26}$$

We take the square of the magnitude as we are dealing with intensity ratios rather than pressure ratios. The normalisation factor N in Equation 22, ensures that this condition is satisfied.

In order to calculate the noise-surface (and therefore noise contours on the ground) of such a source, we need to follow the flyover procedure described previously and calculate the exposure levels at different observer locations.

Combining the definition of the sound exposure level, L_E of Equation 8 and the Spherical Harmonic definition of the directivity function in Equation 22 we have,

$$L_E = 10\log\frac{W(j)C}{NVR}\int_0^\pi \left|\sum_{\ell=0}^{n}\sum_{m=0}^{\ell} A_\ell^m Y_\ell^m(\theta, \varphi)\right|^2 d\theta \tag{27}$$

But, as spherical harmonics are complex functions we have,

$$\left|\sum_{\ell=0}^{n}\sum_{m=0}^{\ell} A_\ell^m Y_\ell^m(\theta,\varphi)\right|^2 = \left(\sum_{\ell=0}^{n}\sum_{m=0}^{\ell} A_\ell^m Y_\ell^m(\theta,\varphi)\right)\left(\sum_{\ell=0}^{n}\sum_{m=0}^{\ell} A_\ell^m Y_\ell^m(\theta,\varphi)\right)^* \tag{28}$$

where the $*$ denotes the complex conjugate.

In order to demonstrate the analytical calculation of the integral in Equation 27, the spherical harmonic expansion has to be truncated, to limit the amount of terms in the product of the complex sum times its conjugate in Equation 28. Therefore, we limit the degree ℓ of the spherical harmonic expansion to just 1. This means that, for this specific demonstration, the directivity function will be built of combinations of a monopole Y_0^0 and the three different dipoles Y_1^0, Y_1^{-1} and Y_1^1. So,

$$\begin{aligned}&\left(\sum_{\ell=0}^{1}\sum_{m=-1}^{\ell} A_\ell^m Y_\ell^m(\theta,\varphi)\right)\left(\sum_{\ell=0}^{1}\sum_{m=-1}^{\ell} A_\ell^m Y_\ell^m(\theta,\varphi)\right)^* = \\ &= (A_0^0Y_0^0 + A_1^{-1}Y_1^{-1} + A_1^0Y_1^0 + A_1^1Y_1^1)(A_0^0Y_0^0 + A_1^{-1}Y_1^{-1} + A_1^0Y_1^0 + A_1^1Y_1^1)^*\end{aligned} \tag{29}$$

Equation 29 results in 16 diagonal and off-diagonal terms containing products of spherical harmonics. Substituting Equation 29 in the integral of Equation 27, the calculation can be broken down into the sum of much simpler integrals, the first integral for example being:

$$\int_0^\pi A_0^0Y_0^0(A_0^0Y_0^0)^*\,\mathrm{d}\theta \tag{30}$$

All 16 of these integrals are similar and their calculation follows the same procedure. Definitions and the theory of spherical harmonics and associated properties may be found in classical works, such as [31, 32]. The integrals may then be simplified into integrals involving combinations of trigonometric functions that can easily be evaluated using techniques such integration by parts.

B. Comparison between analytic and numerical integration of Directivity Functions

The calculation of the integral in Equation 8 has been performed numerically, in order to accommodate discretised directivity data, and analytically (using spherical harmonics) as presented in the previous sections. In order to validate the numerical integration, a few examples are presented below for different directivity functions using combinations of the monopole and the three different dipoles. The figures compare the value of the following integral, for different $D(\theta,\varphi)$. They are presented in polar plots, with the axial variation being in the variable φ.

$$\int_0^{\pi} D(\theta, \varphi)\, \mathrm{d}\theta \tag{31}$$

Figure 6 presents example calculations using the monopole and dipole to define the directivity functions. The result of the integration along the polar angle θ, is a function in φ, the azimuthal angle. The polar plots show how the function varies with φ. In each case the coefficients of the spherical harmonic expansion are presented in matrix form as, $A_\ell^m = [A_0^0\ A_1^{-1}\ A_1^1\ A_1^0]$ to distinguish between the coefficients of different order and degree.

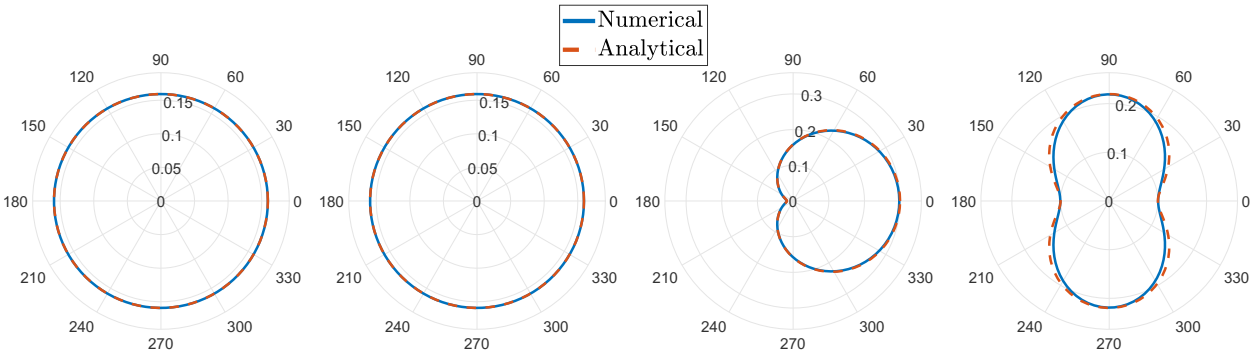

Fig. 6 Comparison of the analytical and numerical calculation of the integral in Equation 27 for four different directivity functions of which the coefficients from left to right are: $A_\ell^m = [1\ 0\ 0\ 0]$, $A_\ell^m = [0\ 0\ 0\ 1]$, $A_\ell^m = [1\ 1\ 0\ 0]$, $A_\ell^m = [1\ 1\ 1\ 1]$.

V. Connections and Contour Area

Once the contour coordinates have been found, the area within the contour is calculated using numerical integration. The regions of the contour where the contributions from two different segments meet are of special interest. In many cases (e.g., turns, power setting changes) discontinuity of the contour arises and the transition from one segment to another is not smooth. The segment interaction error discussed in Section VI is the main cause of the discontinuities. The noise at the observer locations in these regions is heavily influenced by both the preceding flightpath segment and the following one.

In order to model these connecting regions a simple spline was used, defined by points on the contours of both the segments adjacent to the region. These points, also called control points of the spline, are chosen as points on their respective segments where negligible contribution to noise exposure has occurred from other segments (or sound exposure at these points is predominantly due to the aircraft flying along the segment they belong to). The simple splines used are called Bezier curves. They are parametric curves defined by a set of control points. The first, P_0 and last P_n control points are always the end points of the curve; however, the intermediate control points (if any) generally do not lie on the curve. The number of control points also defines the order of the curve (n = 1 for linear, 2 for quadratic, etc.). Figure 7 shows two example calculations where Bezier curves were used to model the segment connection regions.

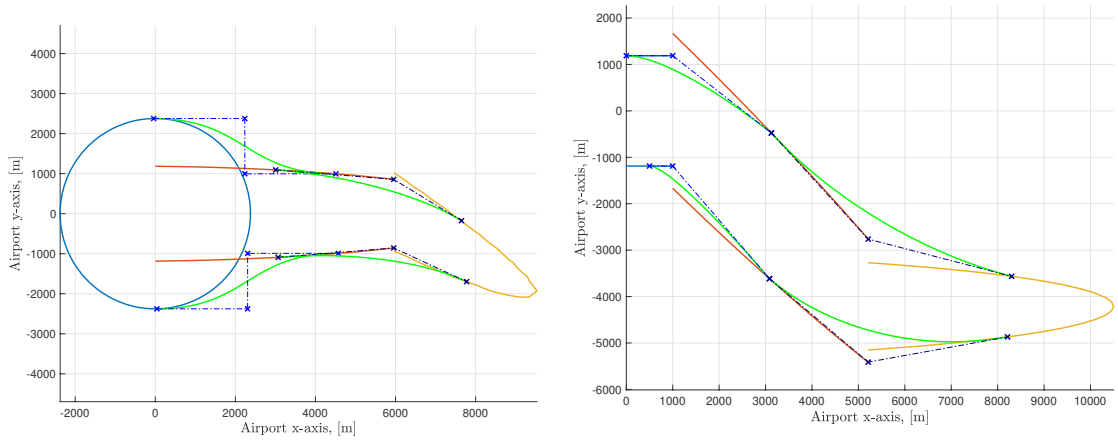

(a) Vertical take-off with turn, 75 dB SEL contour.

(b) Conventional take-off with two turns, 75 dB SEL contour.

Fig. 7 Modeling of connecting regions through the use of Bezier curves. Green lines indicate the Bezier curves; the asterisks indicate the control points, and the blue,red and yellow lines indicate the 2-dimensional contour lines generated as a result of RANE v2 noise surfaces.

For the contour application, the first and last control points are chosen on the contours of the two connecting segments respectively. The order of the curve and therefore the total number of control points is determined by the type of transition between the two segments. It can be seen that in Figure 7 on the left, two types of Bezier curves have been used. The green lines using 4 control points (cubic curve) are modeling the transition from one noise radius to another. While for a turn transition of the same radius, where the contours mostly match up but a slight misalignment occurs, the transition can be modelled using a quadratic (or just three control points) curve, as in the right-hand-side of Figure 7. When a noise radius change occurs, a huge discontinuity in the contour is present.

The exact definition of the locations of the Bezier curve control points is still under investigation. The current implementation uses three main constraints in the positioning of P_0 and P_n:

- P_0 and P_n must be located on the contour lines generated by the two segments of interest. One on each.
- For P_0 and P_n defining a single Bezier curve, the azimuthal locations relative to the corresponding flightpath segments should lie in the same interval, $(-90° < \varphi < 0)$ for the port side or $(0 < \varphi < 90°)$ for the starboard side.
- the resulting curve is tangent to the predicted contour at the points P_0 and P_1, while not intersecting any of predicted contours.
- finally, the location of P_0 and P_1 along the length of each segment is determined based on the location of the corresponding contour's centroid, adjusted by the ratio of two contour areas.

At the moment the only weighting factors used in the definitions of the Bezier curves to manipulate the curvature and slope are to ensure the tangent condition at P_0 and P_1.

It is understood that the implantation of the Bezier curves generally increases area of the predicted contour, as

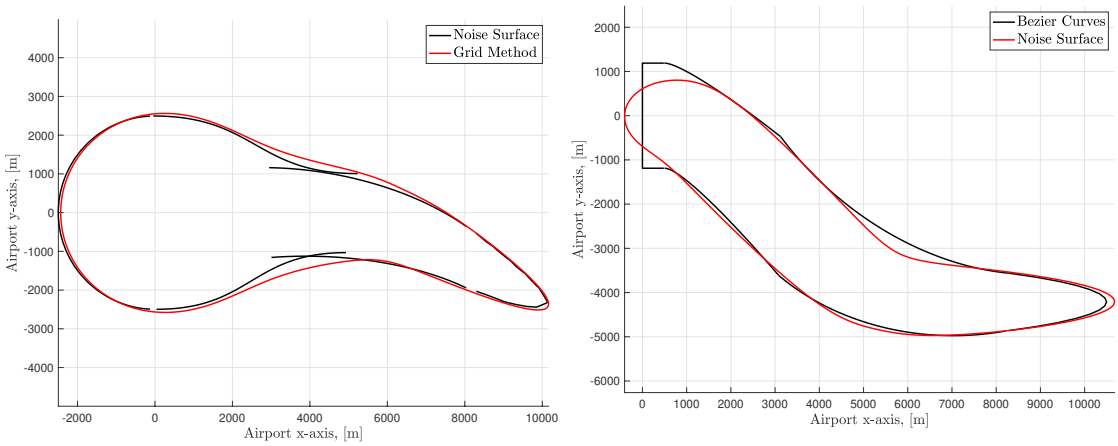

(a) Vertical take-off with turn, 75 dB SEL contour.

(b) Conventional take-off with two turns, 75 dB SEL contour.

Fig. 8 Two different cases of using Bezier curves to approximate segment connections compared to the grid-method (see following Section).

would be expected when correcting for the segment interaction error. In the vast majority of cases, especially the cases used for the bench-marking of RANE v2, the Bezier curve corrections deal with the large discontinuity corrections at the expense of introducing errors, as a result of the control point choice. Smaller errors may occur in the case of complicated directivity (especially static start-of-roll directivity) where possibly introduces smoothing effects. For a real flight path however predictions, using relatively high number of discretisation points (and therefore segments) the discontinuities addressed by the Bezier curves are smaller and less pronounced, counteracting the smoothing effect.

To demonstrate the effectiveness of Bezier curves for the modeling of the connecting regions between segments two different examples are presented in Figure 8, both implementing different combinations of transitions. The contours are compared against an in house grid-point method, introduced in the validation Section VI.

VI. Verification and Validation

To assess the capability of the modifications made to RANE for estimating noise exposure contours and the area within them a multi-step process is required. The initial benchmarking test compares the capability of the RANE v2 model to calculate contours and areas of omnidirectional sources. This was done using an in-house grid-point method. This test was to assess that the original capabilities of RANE were not altered with the addition of non-isotropic sources. To validate the implementation of three-dimensional directivity functions and the connecting region corrections, three case studies of current helicopters will be performed using comparisons against the FAA's AEDT model.

A. Benchmarking against in-house grid-point method

In this section the grid-point model is described and implemented in order to compare sound exposure level contours with the noise surface method developed. The ground surface or airport coordinate system is defined by a Cartesian coordinate system (X, Y, Z) with the runway laying in the $X-Y$ plane. The origin of the coordinate system is positioned at the start of the ground roll with the runway extending out in the positive X direction. In the case of a vertical take-off the origin is again placed at the point where vertical flight is initiated.

Each individual aircraft movement is described by its three-dimensional flightpath, engine power setting and velocity. The flightpath is discretised into simple linear segments defined by a waypoint at the start of each segment. The waypoints carry information that describes the operation and movement of the aircraft along the following segment. The flight parameters, are assumed to remain constant along the length of the segment and are the following: (1) an inclination angle, (2) an angle of rotation, (3) the length of the segment, (4) the engine power setting (or in this case, we define the source as an acoustic monopole emitting noise of some SPL value at the reference distance of 1m) and (5) the speed of the aircraft along the segment [†]. These parameters are almost identical to the ones describing the flightpath of the noise surface method, as the flightpath is the same. Each segment is further discretised into a number of points N_s modeling the movement of the aircraft along this segment.

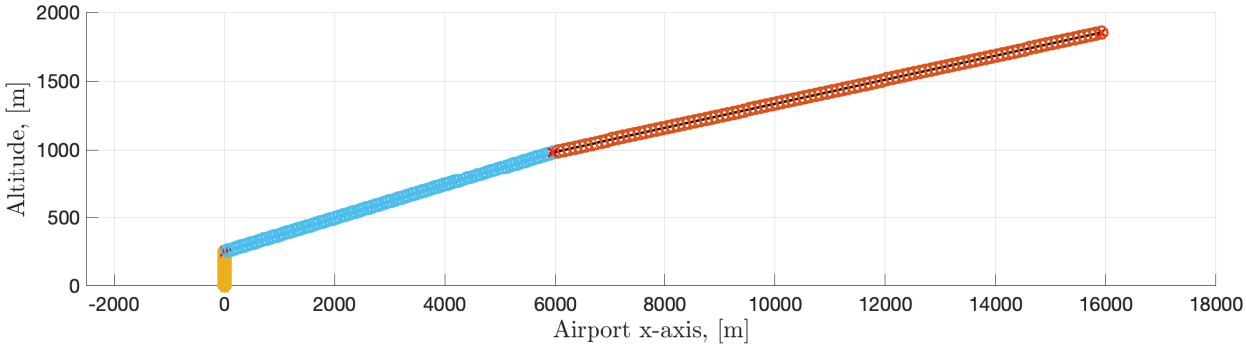

Fig. 9 Discretisation example of flightpath segments for grid-point method. (Yellow) Vertical climb segment, (blue) initial climb to flight level and (red) climb-out at V_y.

At each time step, the aircraft moves to the next point along each segment and the noise due to the lumped noise source is calculated at each of the grid points on the airport ground plane. Using the coordinates of the final point on the last segment of the flightpath an appropriately sized rectangular grid is defined on the ground, $X-Y$ plane. Each point on the grid represents an observer location at which the sound exposure levels of the aircraft movement will be calculated. As the aircraft continues to fly even after the end of the final segment, an extension to the final segment is added. The segment is extended until the acoustic contribution (SPL) to all points on the grid drops close to zero.

The sound level at each grid point due to the aircraft at any point in time is given by:

[†]Accelerated flight is also possible using the noise surface method, and would also result in a quadric noise surface.

$$L_{t,k,i} = L_{p,\text{source}} - 20\log(r) \tag{32}$$

where r is the distance between the specific grid point (observer) and the aircraft at that point in time, and k,i are counters indicating the position of the aircraft along the discretised flightpath. It is important to note that effects such as atmospheric attenuation, lateral attenuation and ground effects are not accounted for in Equation 32. However, this does not skew the comparison to RANE v2 as the equivalent noise radius for each of the segments is calculated through an simulated numerical flyover where the effects of such phenomena are also not accounted for. The comparison between the grid-point method and RANE v2 serves two specific objectives: to prove that total sound power has been conserved after the introduction of the spherical harmonic representation of the directivity factor and that spherical spreading is still accounted for in the calculation of the noise radius. Therefore, as the aircraft flies along the discretised flightpath (assuming $t = 0$ occurs when the aircraft is positioned at the origin for at take-off procedure) the SEL at each individual grid point may be calculated as:

$$\text{SEL} = 10\log\left(\sum_{k=1}^{K}\sum_{i=1}^{N_s} 10^{\frac{Lt_{k,i}}{10}}\Delta t\right) \tag{33}$$

where K denotes the number of segments including the extension to the last segment. Δt is calculated using the aircraft speed along the segments, along with the segment length and number of discretisation points of the segment, N_s. Once the SEL of the single aircraft movement has been calculated at each of the grid point a contour map can be created. An example airport contour map can be seen in Figure 10.

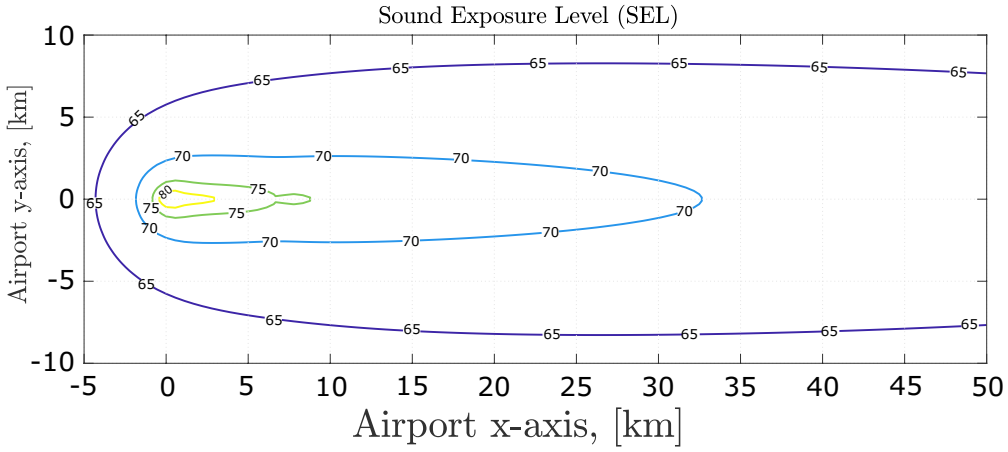

Fig. 10 Example contour map calculation using the grid-method numerical model.

The contour map is composed of multiple contour lines, ranging (in this example) from 60 to 80 dB SEL. The calculation time is highly dependent on the size of the grid and the number of discretisation points in each dimension. The flightpath discretisation also contributes significantly to the computation times. This example computation with

1,000,000 grid points and 100 points along each of the flightpath segments took a total time of 238.258 s. Although excessive, this number of grid-points was chosen to ensure convergence; and as grid-method generation and optimisation techniques are out of the scope of this project, this scale of computation times for simple single runway, 3-5 segment flightpaths examples are manageable for running validation test cases. The equivalent noise surface example was calculated in 36.194 s, almost 6.6 times faster. (NOTE: these calculations were performed on a personal laptop computer, Intel core i7-8850H 8th gen @ 2.60GHz, 16GB RAM).

Table 1 Example input parameter table for conventional and vertical take-off procedures of an omnidirectional noise source.

	Conventional			**Vertical**		
	Segment 1	**Segment 2**	**Segment 3**	**Segment 1**	**Segment 2**	**Segment 3**
Inclination angle, γ (deg)	0.5	7.5	5	90	7.5	5
Rotation angle, ψ (deg)	0	0	0	0	0	0
Segment length, s (m)	1,000	6,000	60,000	100	6,000	60,000
Speed, v (m/s)	100	100	100	1	100	100
Source SPL, L_p (dB)	120	120	120	120	120	120
Noise radius, R (m)	1,110	1,110	1,110	2,000	1,050	1,050

Figures 11, 12 and 13 showcase example calculations using RANE v2 and comparing to the grid-point method, with Figure 13 illustrating an interesting case of a vertical take-off procedure. The input parameters for the case of a simple three segments take-off (Figure 11) are presented in Table 1. Slight alterations to the inputs are made for the cutback and turn examples. All examples assume an omnidirectional source by setting all Spherical Harmonics coefficients to zero other than the monopole term one.

Table 1 also shows the different inputs required for a vertical take-off compared to a conventional fixed wing flightpath. These features were modelled after typical flight profiles and operational procedures of helicopters, operating at helipads according to the FAA [33].

The difference between the two predictions in Figures 11 and 12 occurs for two particular reasons. The first, most obvious, is the lack of a static (or start-of-roll) directivity. This results in an abrupt cut-off of the contour at $x = 0$, with seemingly no noise in the negative side of the airport X-axis. The second is the overestimation by RANE v2 observed in the region between $x = 0$ km and approximately $x = 10$ km. This is primarily due to the finite segment error discussed in more detail in VI.C.1. Segments 1 and 2 are relatively short, therefore the noise radius over an infinite flyover is over-predicted, especially for high SEL noise level contours. For RANE v2 the noise radius remains constant over the length of the segments 1 and 2, whereas in the grid-method observer locations near the start-of-roll experience reduced levels due to the aircraft only moving away from those locations. As we move towards segment 3, $x > 7$ km, which is significantly longer, the match between the two solutions becomes better as the observer locations in this region experience an aircraft flyover which closer resembles that of an infinite flyover.

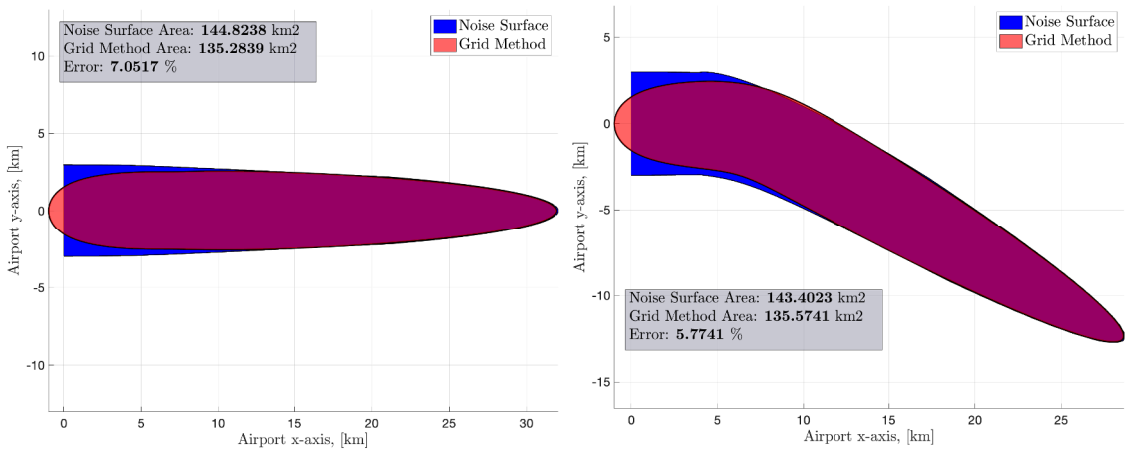

(a) Conventional take-off. **(b) Conventional take-off.**

Fig. 11 The 70 dB SEL contour of an isotropic source. Contour area comparison between RANE v2 (blue) and the grid-point method (red).

An additional error may be observed in Figure 12 in the region of the cut-back (6 < x < 9 km). The transition region in RANE v2 is calculated in this case using the extremities treatment of the unweighted Bezier curves. The position of the control points is a function of the length of the two individual segments where the original discontinuity would arise due to the difference in noise radius, and the noise radius itself. Although the Bezier curves allow for a smooth transition from one segment to another, the gradient of the Bezier curves is not defined, other than the nature of the unweighted cubic Bezier curve and the defined control points. In the case of the grid-method, the contribution to the overall noise by the initial two segments is greater than that of the final (cut-back) segment resulting in the grid-method contour (red) surrounding the RANE v2 contour (blue) in this region. The error is also partially due to both errors discussed in Section VI.C as the control points of the Bezier curves are by definition located on the initial RANE v2 contours, before extremity corrections are applied. Finally, the case presented in Figure 12 represents a rather extreme case where two adjacent segments have a difference in noise radius in the order of 300%. When modeling a more realistic scenario (like the ones presented in Section VI.B) the flightpath is discretised into additional segments, where the flight parameters do not change so drastically.

B. Benchmarking against FAA's AEDT

AEDT is a comprehensive, grid-point model which assesses the noise impact of conventional aircraft fleets around airports, in various metrics, typically noise exposure contours. In addition to conventional fixed wing aircraft, AEDT has the capability of assessing helicopter operations. The Heliport Noise Model (HNM) module was incorporated into INM (Integrated Noise Model) with a helicopter noise database collected through both FAA and manufacturer certification measurements and later into the current version of AEDT.

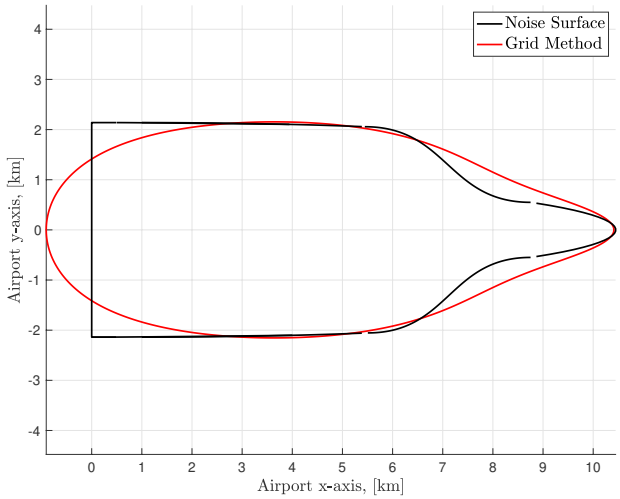

Fig. 12 The 75 dB SEL contour of an isotropic source, conventional Take-off with cutback. Contour area comparison between RANE v2 and the grid-point method.

The decision on using helicopters (or more specifically rotorcraft) as a part of the RANE v2 validation and bench-marking procedure was due to the inherent directional characteristics of such propulsion systems. INM and AEDT differentiate the methodology relative to conventional aircraft for the specific reason of capturing the effects of noise source directivity. As the indented use for RANE v2 is novel aircraft in the regional civil aerospace and UAM (AAM) markets, being able to predict the community noise of the highly in use rotor and propeller propulsion systems, complex source directivity is the main capability being demonstrated.

In order to compare results to AEDT predictions two types of directivities must be specified. First, the start-of-roll directivity function. For helicopters, this directivity correction in AEDT accounts for static radiation patterns that occur while the vehicle is on or slowly ascending vertically from the helipad. To account for this, static directivity data was fitted by a sinusoidal curve fitting model and then decomposed into spherical harmonics. The spherical harmonics expansion was then used as an input for the directivity function on the initial segment of the flightpath. This whole procedure is outline in Figure 14.

Secondly, lateral directivity corrections in AEDT for helicopters are accounted for using 3 NPD curves for every operation, a centre one (directly under the flightpath), a left one ($\varphi = -45°$ with respect to the flightpath) and a right one ($\varphi = 45°$). Examples of the constant speed departure NPD's of the Boeing Vertol may be seen in Figure 15 (left). All levels at azimuthal angles between the left and centre curves are interpolated logarithmically (the same applies for all values of φ between the right and centre). For values of $\varphi > 45°$ and $\varphi < -45°$ the level at the right ($\varphi = 45°$) is taken and for the left hand side NPD respectively.

In order to generate a directivity function suitable for RANE v2, the three distances at the sound exposure (in the case of the example Figure 15, 55 dB SEL is chosen) of interest were used to generate a polynomial curve fitting for

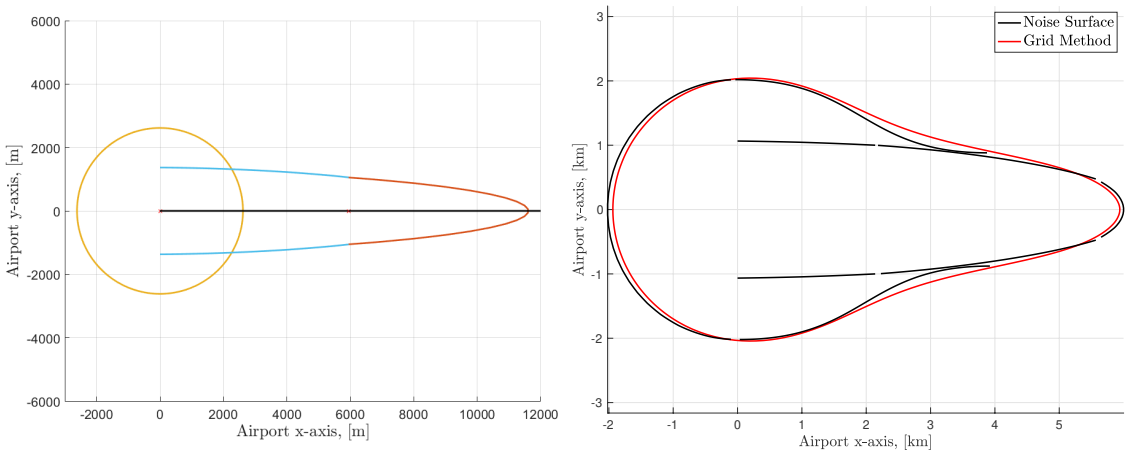

(a) RANE v2 set-up and contour lines with flightpath indicated in black.

(b) Comparison between RANE v2 and the grid-point method of the 75 dB SEL contour.

Fig. 13 Isotropic source during vertical take-off.

all values of φ between $-90°$ and $90°$, Figure 15. The black crosses on the right-hand-side of Figure 15 represent the distance obtained by the green crosses on the NPD's (left), referenced to the distance of the center NPD. The correction $\Delta R(\varphi)$, is then used along with the nominal center NPD to generate the required noise surface and contour.

It is worth noting that the polynomial fit in Figure 15 is an aid that allows the fitting of a spherical harmonic expansion to a function that otherwise has a discontinuous first derivative. It is not an exercise in attempting to replicate or extending the lateral corrections used by AEDT. The discontinuous nature of the correction, as it is implemented by AEDT, would result in multiple high order modes being required in the spherical harmonic expansion to capture those discontinuities. The AEDT methodology for lateral correction is in itself an simplifying assumption as well as a compromise, that balances the need of applying a lateral correction, and the cost and time expense of generating lateral NPD curves for all applicable helicopter and air vehicles. The largest errors introduced are at the extremities and beyond of the domain of interest ($\varphi \approx \pm\pi/2$), at which point the noise is not radiated to the ground.

Three helicopter models were used in this comparison, to cover three different weight (size) groups. The Schweiser 300C, a light utility helicopter, the Eurocopter AS365 Dauphin, a medium sized also utility helicopter; and the Boeing CH-47 Chinook, a large transport helicopter. The default helicopter flight profile from AEDT 3c was used along with a default linear flight track. The total flightpath is broken down into four major segments: a. A vertical take-off, b. a horizontal acceleration, c. a climb to altitude and d. a horizontal steady level flight. These are also the segments used to model the take-off operation in RANE v2. The resulting contour comparison for all three helicopters may be seen in Figure 16.

Finally, Figure 17 shows a contour map comparison for the Boeing CH-47 Chinook. The map includes sound level of 75 dB, 65 dB and 55dB. RANE v2 again matches the AEDT prediction very well, however it is evident that the error increases as we look at lower SEL levels.

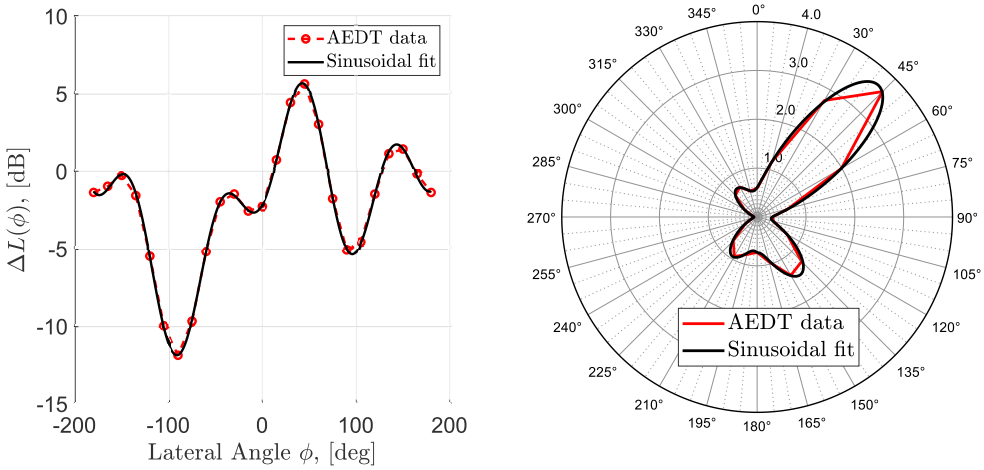

(a) Static directivity index, DI [dB] pattern of the Boeing CH-47 Chinook. (Left) Cartesian plot showing the raw AEDT data [12, 13, 24] and a polynomial fit. (Right) Polar plot of the same data and fit in the form of a direcitivty factor, D [-].

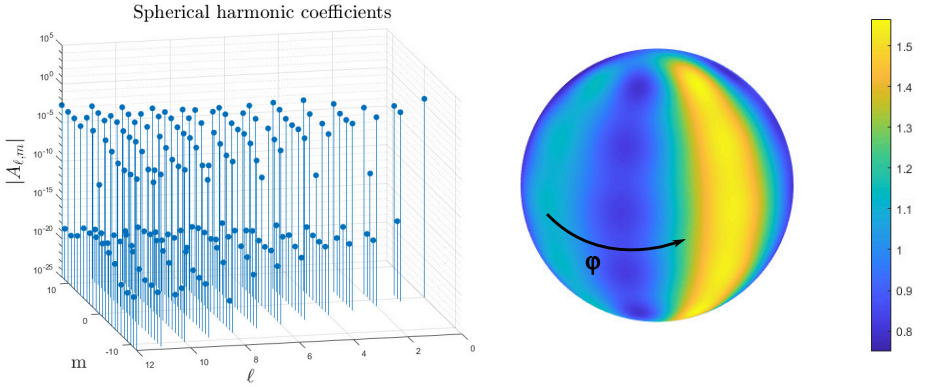

(b) (Left) magnitude of the spherical harmonic expansion coefficients for the static directivity data fit of Figure 14a. (Right) Spherical harmonic representation of the static directivity on a spherical colour-map plot. Output of Equation 22.

Fig. 14 Procedure of treating numerical data as inputs to RANE v2. The output spherical harmonic expansion of Figure 14b is then used to generate the required noise surfaces.

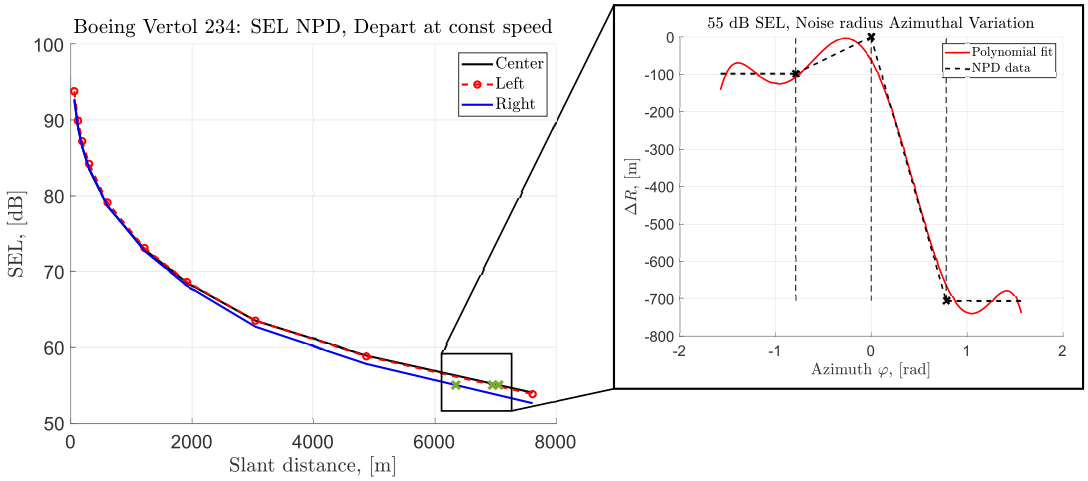

Fig. 15 (Left) SEL Noise-Power-Distance curves for the Boeing Vertol 234 for a constant speed departure. The three curves indicate three lateral location of observers. The green crosses indicate the intersection of the 55 dB SEL line with the curves. These points are used to generate a polynomial function that describes the variation in the azimuthal direction (Right).

Overall RANE v2 matches the contours generated by AEDT. Slight errors in the static directivity prediction (occurring in the first segment, around the $(0, 0)$ origin of the airport plane) are due to curve fitting errors and the truncation of the spherical harmonic expansion to only $\ell = 12$. Errors associated with the noise surface method itself are described in the following Section.

C. Sources of Error

1. Finite Segment Error

The model of RANE and subsequent update RANE v2, assumes that sound exposure surfaces are formed around the flightpath as the aircraft flies from $-\infty$ to $+\infty$. These surfaces are then positioned around the segments of a discretised version of the actual flightpath the aircraft takes during take-off and landing operations. As long as these segments are of significant length, where the contribution of the remaining parts of the infinite segment are negligible compared to the actual segment itself, the error in the actual position of the contour, and therefore the noise radius itself should also be negligible. The shorter the discretised segment of the flightpath is, the less of a contribution it has compared to the infinite flyover the noise surface was calculated with. As the segment length $s \longrightarrow \infty$, the noise emission corresponding to the segment tends to the noise in the equivalent NPD data set. An error is introduced when the limit is not satisfied, meaning a short segment is being considered.

This error can be dealt with by altering the limits of integration when calculating the directivity function. Instead of assuming the aircraft flies along an infinitely long flightpath, meaning the integration limits in terms of the variable θ are 0 to π; for each segment the aircraft flies along a flightpath equal to the segment length. This requires that the new limits of integration for the noise surfaces are within the old ones (i.e., 0 < lower limit and upper limit < π), and the

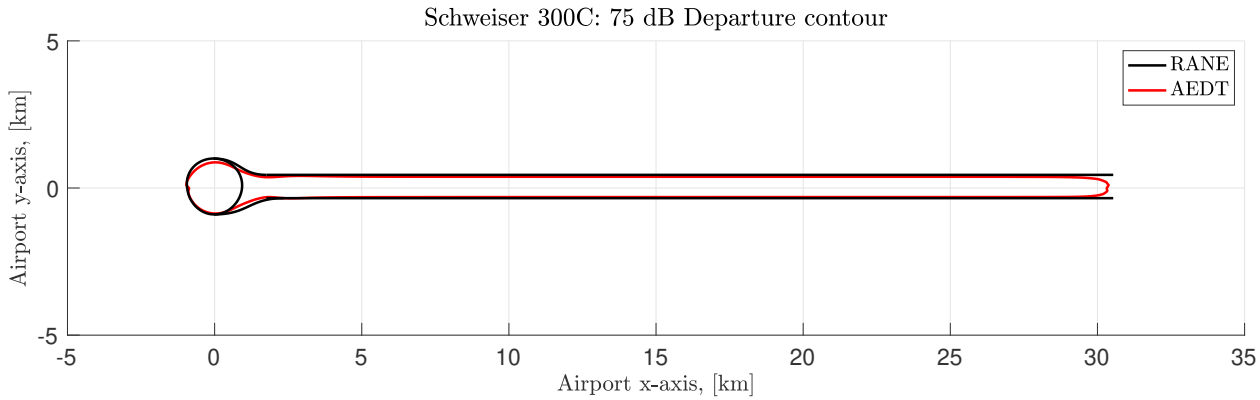

(a) Schweiser 300C

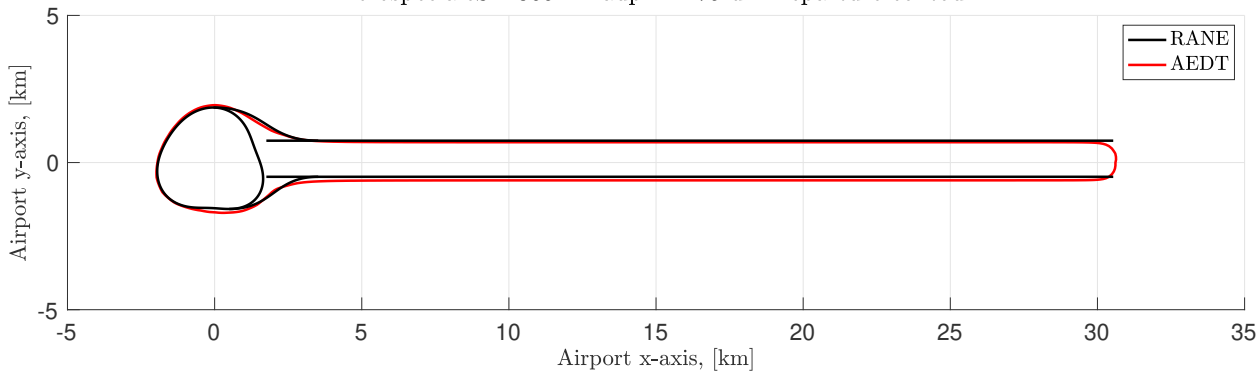

(b) Eurocopter AS365 Dauphin

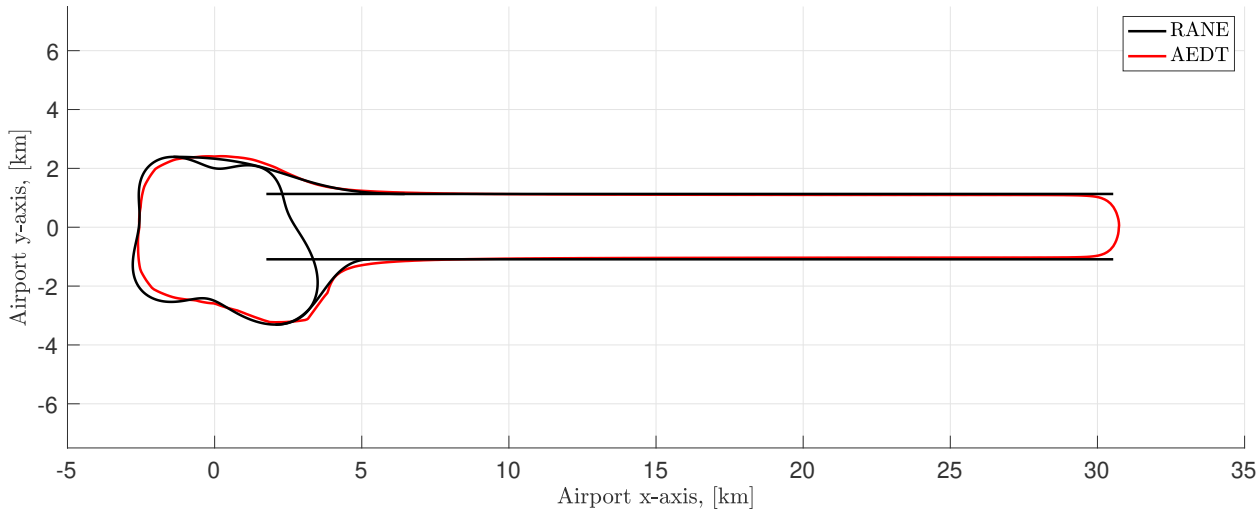

(c) Boeing CH-47 Chinook

Fig. 16 Comparison between the RANE v2 and AEDT 3c prediction for three different helicopters.

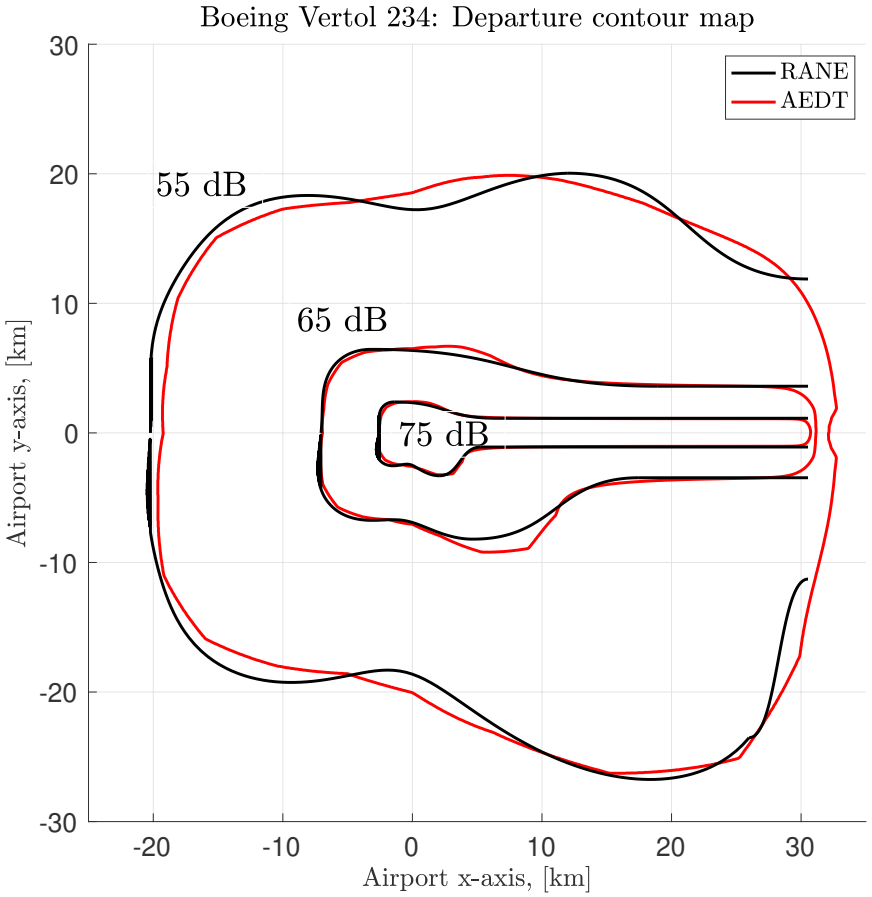

Fig. 17 SEL noise exposure contour map for Boeing CH-47 Chinook. Comparison between AEDT and RANE predictions.

interval is, therefore, of smaller length. The procedure of calculating the correction factor is outlined in Appendix E of Doc29 Volume 2 [11].

The implementation of the finite segment correction within RANE v2, follows the methodology suggested by Doc29 with one significant difference. The source directivity used for the calculation of the correction is no longer the assumed 90° dipole source that varies proportionally to $\sin^2\theta$. Instead the correction is calculated using the spherical harmonic expansion of the three-dimensional source, leading the sound exposure at the observer from the flyover being proportional to the integral,

$$\int_{t_1}^{t_2} \frac{WD(\theta,\varphi)}{r^2} C \, \mathrm{d}t \tag{34}$$

where t_1 and t_2 define the time interval during which the aircraft is flying within the finite segment of length s; $D(\theta,\varphi)$ is given by Equation 22. The integral can be calculated analytically in a similar way to the procedure in Section IV.A or through numerical integration.

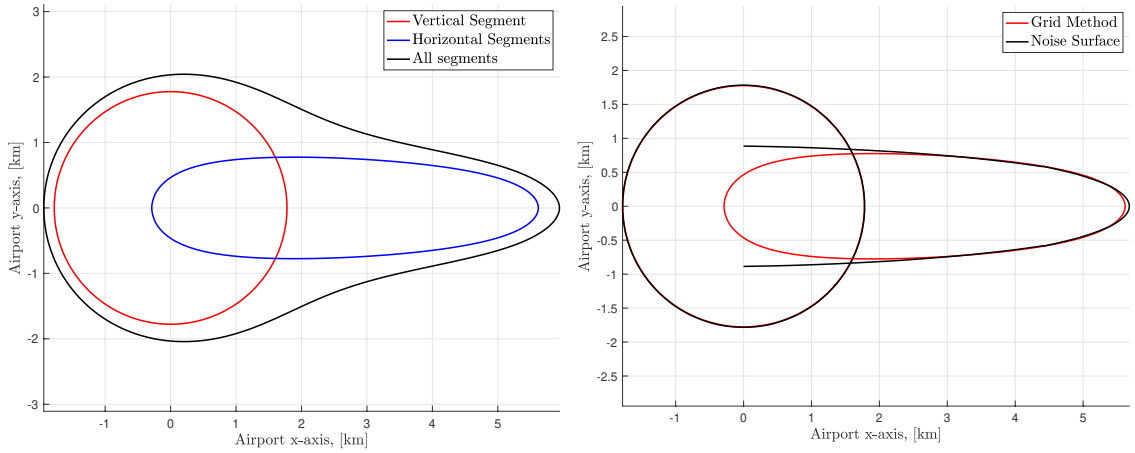

(a) Grid-point method 75 dB SEL contour: Comparison between the vertical and horizontal segment individual calculations and the total flightpath calculation.

(b) Comparison between RANE v2 and the grid-point method when calculating the vertical and horizontal segments individually.

Fig. 18 Demonstration of segment interaction error using results from the grid-method and RANE v2.

2. Segment interaction error

An error arises in the calculation of the noise radius for the noise surface method. The noise radius for each individual segment is calculated using NPD curves for a specific power setting, speed and sound exposure level. NPD curves assume a steady level fly-over a single observer from effectively $-\infty$ to $+\infty$ for the calculation of the exposure levels. Therefore, for any given point on the contour, the noise is due to one segment alone. The contribution of all other segments to that specific contour is neglected; this causes the noise segment method to underestimate the noise radius, as contributions from other segments would increase noise exposure at these observer locations causing the contour to move further away from the flightpath.

To demonstrate this, two tests were performed. One was using the grid method alone, where a vertical take-off operation was modelled in two different ways. (a) All segments of the flightpath contributed to the calculation of the exposure contour maps and (b) the vertical segment of the flightpath was calculated separately than the two horizontal ones. The result can be seen in Figure 18a. The black line indicates the contour generated when all segments of the vertical take-off (meaning vertical and horizontal) where taken into account in the estimation of the SEL on the ground. The contour is of significantly larger area relative to the combined area of the blue and red contours, disregarding the overlap. This is due to the contributions of all segments to the sound exposure level when generating the black contour, whereas the blue and red contours were generated independently only taking into account in each case the vertical and horizontal segments respectively.

To further illustrate the point, the noise surface method used by RANE v2 (before the extremity and connecting region treatments are applied) is compared to the grid-point method contour calculation of Figure 18a where the vertical and horizontal parts have been calculated separately. This is shown in Figure 18b. The match is clearly much

better. Comparing the black lines in Figures 18a and 18b demonstrates the importance of introducing the Bezier curve corrections in RANE v2, especially to the connecting regions between contours. Future work on expanding the capabilities of RANE beyond single runway airports and will introduce a correction factor ΔR to the calculation of the noise radii of all segments to account for the presence of other contributing segments. However this is out of the scope of this work.

VII. Conclusion

This paper presents RANE v2, the second version of the airport noise model. This update allows for the definition of complex, realistic, three-dimensional directivity patterns in a numerically efficient way, useful for assessing the noise impact of novel aircraft such as VTOL rotorcraft and UAM air vehicles as well convectional fixed wing aircraft. The useful analytical properties of spherical harmonics allow for a closed-form solution for the generation of noise exposure surfaces and contours to be reached. Combined with the pre-integrated nature of the segmentation methodology adopted by RANE v2, rapid assessment of single runway scenarios for single or multiple noise events is possible. The inclusion of a fully three-dimensional directivity captures the variation in the shape of the noise contour relative to that of an isotropic noise source. These change in location and area of the contours can help identify possible hazardous locations around airport/vertiports that may require further noise abatement procedures to be considered. RANE v2 is intended as a high-level airport noise tool that can help bridge the gap between aircraft conceptual design and aviation community noise. It allows the possibility of being integrated in the design workflow due to the reduced requirement for inputs data and fast computation turnaround times. Future technologies, scenarios, and aircraft design spaces in the form of parametric studies can be explored. The tool provides the connection between designers, airport strategic planners and their impact on communities through guiding the decision-making process.

The introduction of a directivity function to describe the three-dimensional emission patterns of real aircraft was validated in two specific ways. The first comparisons against the in-house grid point method, conformed that acoustic energy is preserved over the flyover procedure. Contour predictions for simple turns, cut-back procedures and vertical take-off provided proof that the Bezier curve treatment to extremities and connecting regions provides a simple, yet highly effective method for interpolating between contour segments and eliminating discontinuities. Decrease in the error of contour area prediction were also observed. Secondly, RANE v2 was benchmarked using three realistic case studies. The air vehicles of choice were helicopters, due to the inherent high directivity. Comparisons with the AEDT helicopter module for three different sized helicopters, the Schweiser 300C, the Eurocopter AS365 Dauphin and the Boeing CH-47 Chinook were performed and discussed. Two different examples of input data were used in order to generate the required directivity function as input to RANE v2. The presented case studies provide reassuring evidence that the framework can provide predictions and may be integrated within design systems of UAM and AAM (Advanced Air Mobility) air vehicles to help minimise the impact of such vehicles on community noise.

The two main phenomena affected by the introduction of a fully anisotropic source are lateral attenuation and lateral directivity. The definition of the aircraft as a lumped three-dimensional source, along with the full procedure of performing the flyover integration, allows for treatment of these effects to be corrected on a source basis and be included on the full description of the three-dimensional source in terms of the spherical harmonic expansion. This overcomes the need to apply further corrections at each individual observer location as they are automatically captured in the generation of the specific noise surfaces. Empirical corrections such as the ones provided by the ECAC Doc 29 methodology may be used in analytical form, but may be substituted when case specific data is available.

The importance of capturing the specific locations of the noise exposure contour lines, though the use of directivity functions, is highlighted when combining them with the geographic distributions of resident populations around airports. RANE v2 can be applied to airport/vertiport specific cases or simplified UAM networks, to compute noise contours, and provide insight on the direct effect the radiation patterns have on the community on the ground. ATC movements and flightpath are strongly influenced by the noise reaching the residing population around the operating air vehicles. Preliminary route planning according to noise emissions can be performed using RANE v2, whilst guidance on particular components influencing the contour patterns can be fed-back to the manufacturers as a part of conceptual design.

On an aircraft level, assessment of individual noise source directivity effects on noise contours, allow the exploration of engine installation, reflection and blockage effects to maximise the potential benefits on noise exposure. The incorporation of directivity effects may then be coupled with models for generating NPD curves for novel aircraft [34, 35] and therefore predicting the PWL outputs, to provide global assessment of the noise impact of new technology and/or implementation of noise abatement operational procedures.

A more general problem that the current version of RANE does not address is the dependence of directivity on frequency. The use however, of the spherical harmonic representation of a source allows the methodology to be easily extendable to account for this frequency dependence. Assuming for example a $1/3^{rd}$ octave source spectrum, each individual band could be allocated a three-dimension directivity function in the form of a spherical harmonic expansion. The lumped source directivity would then be given, by not only the sum over the individual source directivity but also the sum over the directivity of each frequency band. This implementation forms part of the future work. The use of a single lumped source directivity for all spectral bands conforms with the methodology within ECAC Do29, the ANP database and computational methodology within SAE-AIR 1845 [22] for the generation of NPD curves, and extends it to lateral location with the inclusion of azimuthal directivity.

Combining the capabilities of RANE v2 with those of the original RANE model, improved assessment of single runway, single event or fleet movements is possible. The assumption of no change in the spatial distribution of flight tracks presents limitations to the modeling capability. This shortcoming is planned to be addressed in future developments, including power setting and aircraft speed variation, through the derivation of appropriate noise surfaces.

Acknowledgments

References

[1] 2022.

[2] "Future flight," , Aug 2022. URL https://ktn-uk.org/transport/future-flight/.

[3] "FlyZero reports archive," , ???? URL https://www.ati.org.uk/flyzero-reports/.

[4] Gohardani, A. S., "A synergistic glance at the prospects of distributed propulsion technology and the electric aircraft concept for future unmanned air vehicles and commercial/military aviation," *Progress in Aerospace Sciences*, Vol. 57, 2013, pp. 25–70.

[5] Gohardani, A. S., Doulgeris, G., and Singh, R., "Challenges of future aircraft propulsion: A review of distributed propulsion technology and its potential application for the all electric commercial aircraft," *Progress in Aerospace Sciences*, Vol. 47, No. 5, 2011, pp. 369–391.

[6] Rendón, M. A., Sánchez R, C. D., Gallo M, J., Anzai, A. H., et al., "Aircraft hybrid-electric propulsion: Development trends, challenges and opportunities," *Journal of Control, Automation and Electrical Systems*, Vol. 32, No. 5, 2021, pp. 1244–1268.

[7] Brelje, B. J., and Martins, J. R., "Electric, hybrid, and turboelectric fixed-wing aircraft: A review of concepts, models, and design approaches," *Progress in Aerospace Sciences*, Vol. 104, 2019, pp. 1–19.

[8] Rizzi, S. A., Huff, D. L., Boyd, D. D., Bent, P., Henderson, B. S., Pascioni, K. A., Sargent, D. C., Josephson, D. L., Marsan, M., He, H. B., et al., "Urban air mobility noise: Current practice, gaps, and recommendations," Tech. rep., 2020.

[9] Goyal, R., "Urban Air Mobility (UAM) Market Study," Tech. rep., National Aeronautics and Space Administration (NASA), November 2018.

[10] "Vertiports: Prototype Technical Specifications for the Design of VFR Vertiports for Operation with Manned VTOL-Capable Aircraft Certified in the Enhanced Category," Report no. pts-vpt-dsn, European Union Aviation Safety Agency (EASA), March 2022.

[11] "Report on standard method of computing noise contours around civil airports, vol. 2: Technical guide," Tech. rep. ecac.ceac doc. 29, 4th ed, European Civil Aviation Conference (ECAC), December 2005.

[12] Centre, E. E., "Aircraft noise and performance (ANP) database v2.1," , 2016. URL http://www.aircraftnoisemodel.org.

[13] Koopmann, J., Hansen, A., Hwang, S., Ahearn, M., and Solman, G., "The CAA aircraft noise contour model: ANCON version 1," Tech. rep. dot-vntsc-faa-16-17, Federal Aviation Administration (FAA), July 2016.

[14] Nuic, A., Poles, D., and Mouillet, V., "BADA: An advanced aircraft performance model for present and future ATM systems," *INTERNATIONAL JOURNAL OF ADAPTIVE CONTROL AND SIGNAL PROCESSING*, 2010.

[15] Ollerhead, J., "The CAA aircraft noise contour model: ANCON version 1," Tech. rep. dora 9120, Civil Aviation Authority (CAA), January 1992.

[16] Torija, A. J., Self, R. H., and Flindell, I. H., "A model for the rapid assessment of the impact of aviation noise near airports," *The Journal of the Acoustical Society of America*, , No. 2, 2017, pp. 981–995.

[17] Smith, M. J. T., *Aircraft Noise*, Cambridge University Press, 1989.

[18] Stewart, E. C., and Carson, T. M., "Simple method for prediction of aircraft noise contours," *J. Aircraft*, 1980, pp. 828–830.

[19] Levy, S., "Geometry formulas and facts," *http://www. geom. umn. edu/docs/reference/CRC-formulas*, 1995.

[20] "Metrics for Aircraft noise," Ercd report 0904, CAA, January 2009.

[21] Synodinos, A. P., "A new framework for estimating noise impact of novel aircraft," Ph.D. thesis, University of Southampton, 2017.

[22] "Society of Automotive Engineers: Procedure for the Calculation of Aircraft Noise in the Vicinity of Airports," Tech. Rep. 1845, SAE AIR, 1981.

[23] "AIR-5662," Tech. rep., Society of Automotive Engineers, 2006.

[24] Koopmann, J., Hansen, A., Hwang, S., Ahearn, M., and Solman, G., "Aviation environmental design tool (AEDT) version 2c technical manual," Tech. Rep. Tech. Rep. DOT-VNTSC-FAA-16-17, Federal Aviation Administration (FAA), July 2016.

[25] Rizzi, S., and Rafaelof, M., "Community noise assessment of urban air mobility vehicle operations using the FAA Aviation Environmental Design Tool," *INTER-NOISE and NOISE-CON Congress and Conference Proceedings*, Vol. 263, Institute of Noise Control Engineering, 2021, pp. 450–461.

[26] Li, J., Ng, H. K., Zheng, Y., and Gutierreznolasco, S., "Noise Exposure Maps for Urban Air Mobility," *AIAA AVIATION 2021 FORUM*, 2021, p. 3203.

[27] Brentner, K. S., Bres, G. A., Perez, G., and Jones, H. E., "Maneuvering rotorcraft noise prediction: A new code for a new problem," *Ahs aerodynamics, acoustics and test evaluation specialist meeting*, 2002.

[28] Goldman, B. A., "Modifications to PSU-WOPWOP For Enhanced Noise Prediction Capabilities," 2012.

[29] "Integrated aircraft noise and emissions modelling platform (impact)," , ???? URL `https://www.eurocontrol.int/platform/integrated-aircraft-noise-and-emissions-modelling-platform`.

[30] INECO, P. L., and ISDEFE, E., "EPISODE 3," ????

[31] Müller, C., *Spherical Harmonics*, Lecture notes in mathematics, Springer-Verlag, 1966. URL `https://books.google.co.uk/books?id=A9UQAQAAIAAJ`.

[32] Freeden, W., and Schreiner, M., *Spherical Harmonics, Splines, and Wavelets*, Springer Berlin Heidelberg, Berlin, Heidelberg, 2019, pp. 1–47. https://doi.org/10.1007/978-3-662-46900-2_101-1, URL https://doi.org/10.1007/978-3-662-46900-2_101-1.

[33] "Helicopter Noise Exposure curves for use in Environmental impact assessment," Tech. rep. report no. faa-ee-82-16, Federal Aviation Administration (FAA), November 1982.

[34] Synodinos, A. P., Self, R. H., and Torija, A. J., "A framework for predicting Noise-Power-Distance curves for novel aircraft designs," *Journal of Aircraft*, 2017.

[35] Amargianitakis, D., Self, R. H., Proença, A. R., Synodinos, A. R., and Torija, A. J., "Towards predicting noise-power-distance curves for propeller and rotor powered aircraft," *INTER-NOISE and NOISE-CON Congress and Conference Proceedings*, Vol. 263, No. 3, 2021, pp. 3909–3920. https://doi.org/doi:10.3397/IN-2021-2555, URL https://www.ingentaconnect.com/content/ince/incecp/2021/00000263/00000003/art00105.

Closed-form analytical approach for calculating noise contours of directive aircraft noise sources

Amargianitakis, Daniel C.

2023-03-09

Amargianitakis DC, Self RH, Synodinos AP, et al., (2023) Closed-form analytical approach for calculating noise contours of directive aircraft noise sources. AIAA Journal, Volume 61, Issue 4, April 2023, pp. 1735-1748

https://doi.org/10.2514/1.J062033